Final Report

Improvements of Intelligent Electronics System Research Laboratory in the Second Phase

Under a Research Grant No. A56-3-3-3

Assistant Professor Dr Wimol San-Um

Intelligent Electronics Systems Research Laboratory

Master of Engineering Technology Program

Faculty of Engineering, Thai-Nichi Institute of Technology

Exclusive Summary

The final report of a research project on "Improvements of Intelligent Electronics System Research Laboratory in the Second Phase" is presented. This project mainly aims to implement an electronics work station of IES research laboratory and purchase high-technology equipment for supporting research and study in both bachelor and master courses. Additionally, this project also accelerates publication on intelligent devices, communications, and electrical engineering, and prepares knowledge as well as knowhow to be ready for industrial services. This report provides a result of research operations under the research grant no. A56-3-3-3 as follows;

First, the infrastructure and high-technology equipment have been implemented and purchased, including the workbench stations for electronics experiments, high-performance computers, mini-CNC machine, network analyzer, digital multi-meter, and acoustic emission system. All these device and machines have been exploited for research and academic services for both undergraduate and graduate students in various courses, such as CPE-203 Engineering Electronics, CPE-311 Embedded Systems or CPE-400 Artificial Intelligences.

Second, three research themes are presented, i.e. (i) an intelligent acoustic emission, (ii) intelligent feedback control system, and (iii) intelligent nonlinear dynamic systems for secure communications and data storage. Such research themes have responded to the need of master students who brought research problems from their workplaces to conduct a research at IES laboratory.

Last, the outputs of research operation are not only publication of research papers but also academic services to industrial sectors. There have been two refereed international journals and some conference papers counted as KPI in terms of publications for TNI. In addition, all facilities have been used for the academic service in cooperation with the department of industrial promotion, ministry of industry.

Acknowledgements

The author wishes to express his profound gratitude and to respectfully dedicate this work to his parent and family members for their endless encouragements, love and sacrifices. The author is most grateful to Research and Academic Services Division, Thai-Nichi Institute of Technology for financial supports. Grateful acknowledgements are also made to the president and the vice president of Thai-Nichi Institute of Technology for continuous supports for IES Laboratory. In addition, The author wishes to acknowledge Faculty of Engineering, involving Dean and Associate Dean along with colleagues for inspiration and technical assistances. The author sincerely appreciates LSI lab members for their useful technical experience sharing and kind technical assistance.

Table of Contents

List of Figures

List of Tables

1. INTRODUCTION

This report is a result of a research project on "Improvements of Intelligent Electronics System Research Laboratory in the Second Phase" under a research grant no. A56-3-3-3 with a financial support of 1,000,000 Baht. This research project has the following objectives;

(1) To implement an electronics work station of IES research laboratory and high-tech equipment for supporting research and the study in master course

(2) To produce the publication on intelligent devices, communications, and electrical Engineering

(3) To improve IES research laboratory to be ready for industrial services.

2. IMPROVEMENTS OF INFRASTRUCTURE AND RESEARCH EQUIPMENT.

2.1 Durable Articles for IES laboratory infrastructure

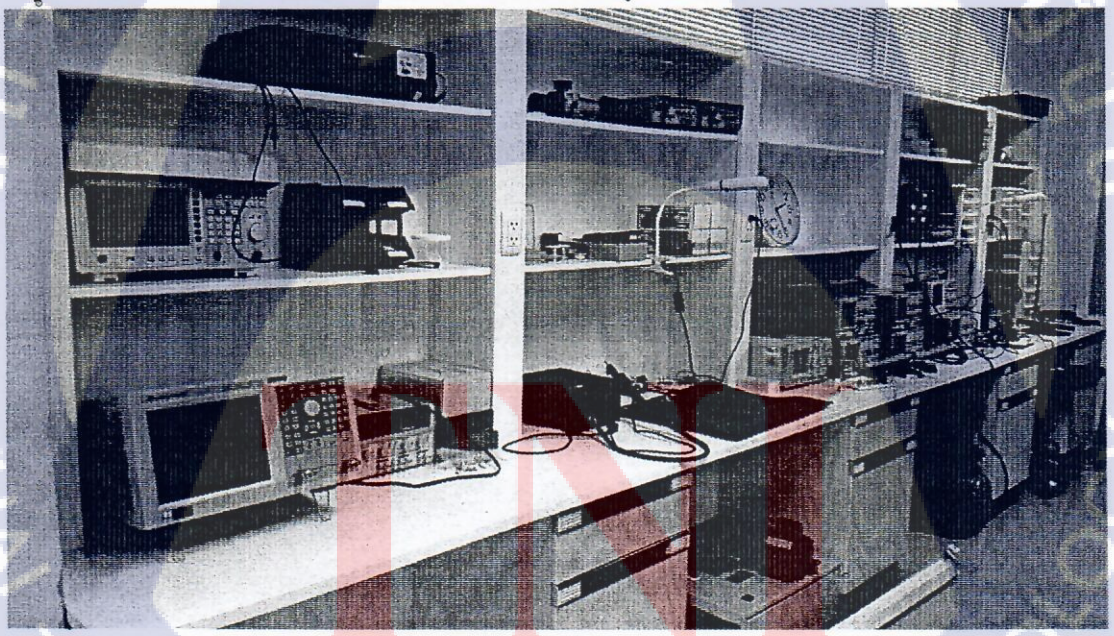

Figure 2.1 The workbench stations for electronics experiments.

2.2 Durable Articles for Research Equipment

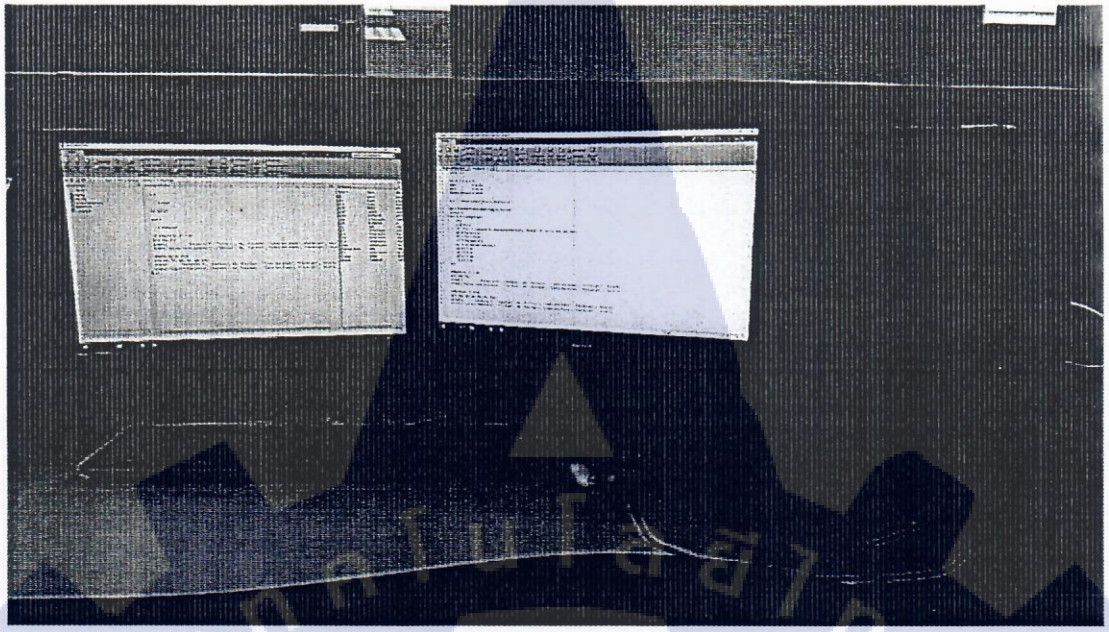

Figure 2.2 High-Performance Station 1 for MATLAB Simulations.

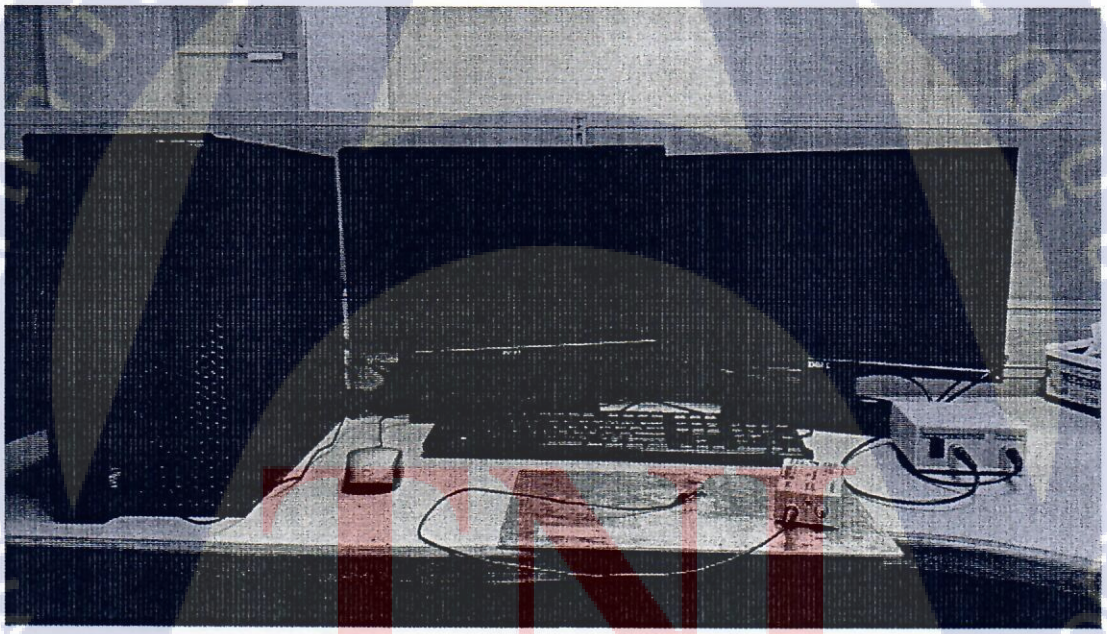

Figure 2.3 High-Performance Station 1 for LABVIEW Simulations.

Figure 2.4: Computer station 3 iMAC for Graphic Designs.

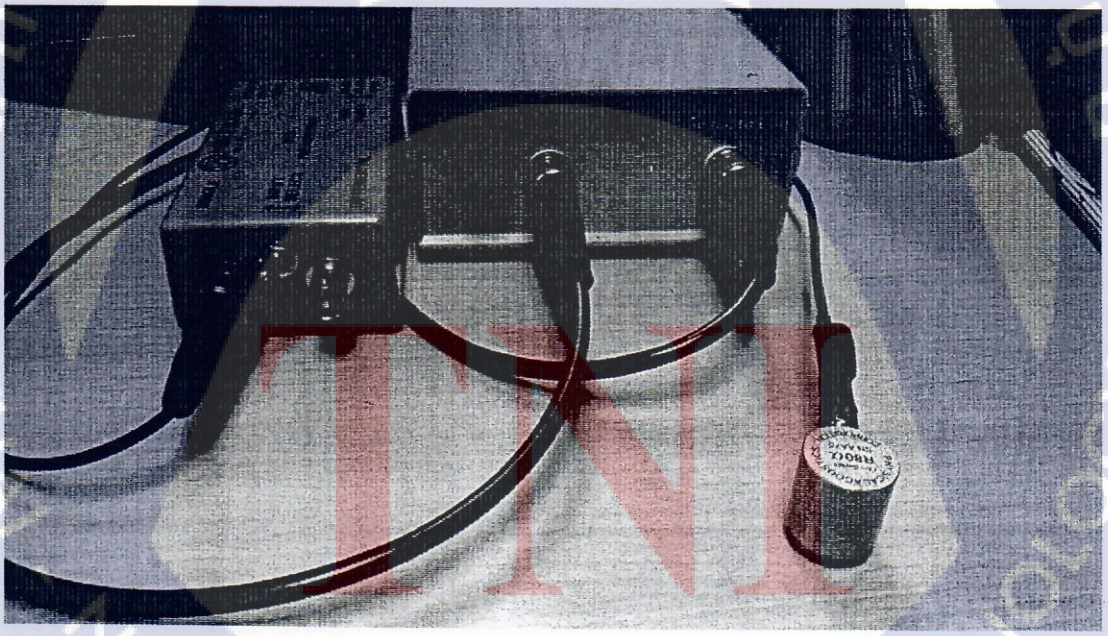

Figure 2.5 : Acoustic Emission Sensor and its Preamplifier.

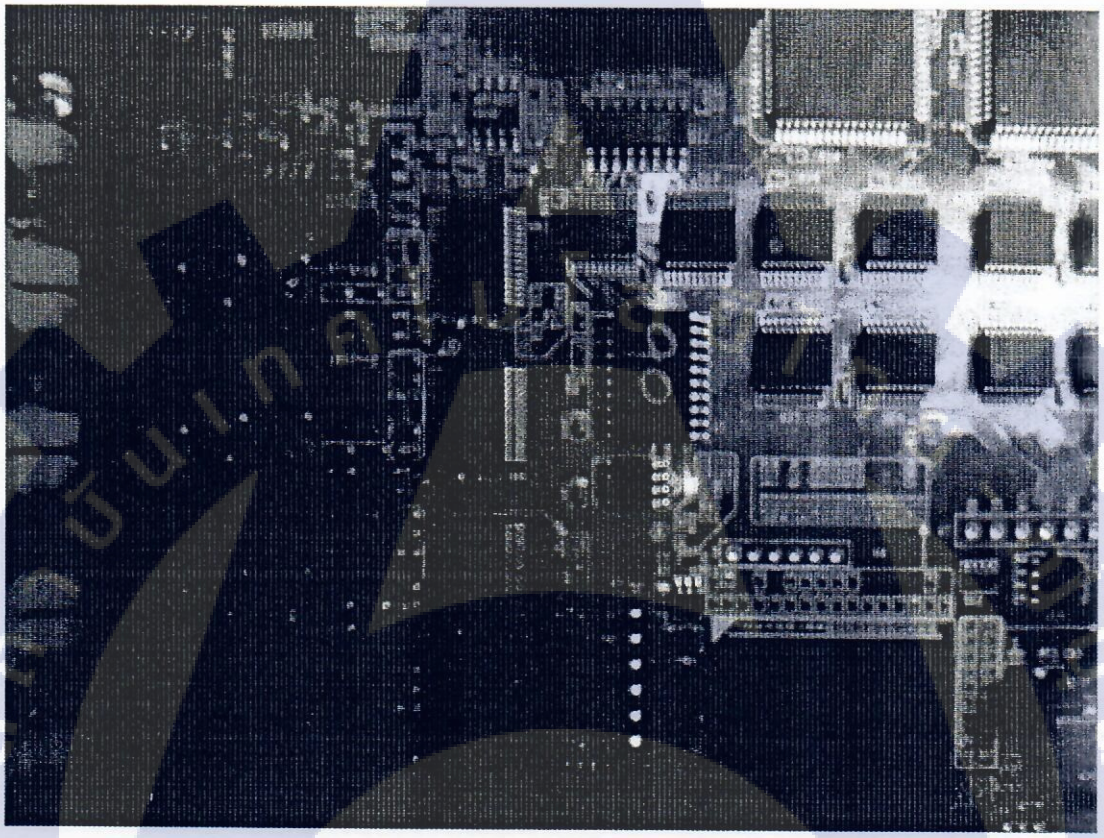

Figure 2.6 : Data acquisition board for Acoustic Emission Sensor.

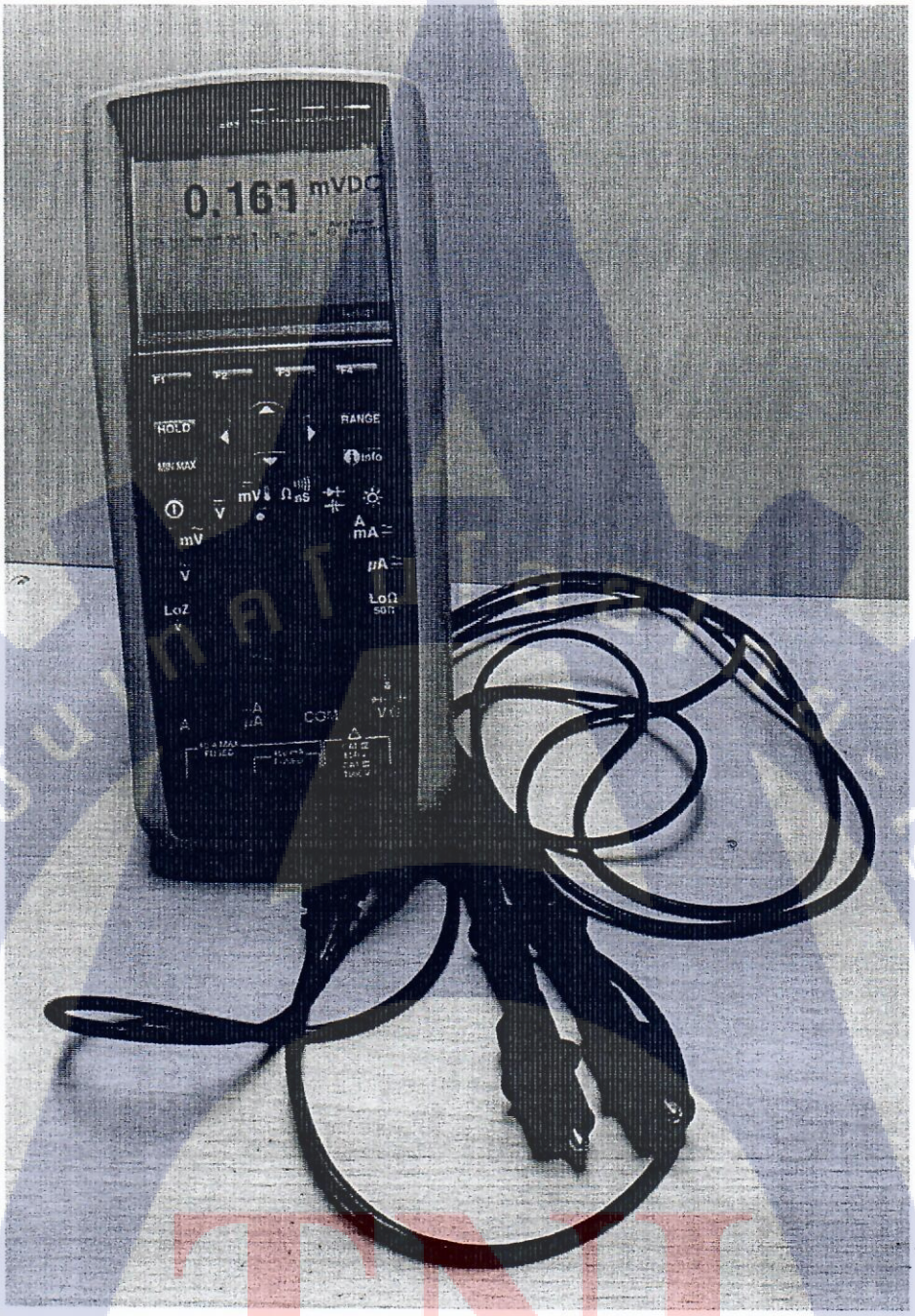

Figure 2.7: Digital Multi-Meter.

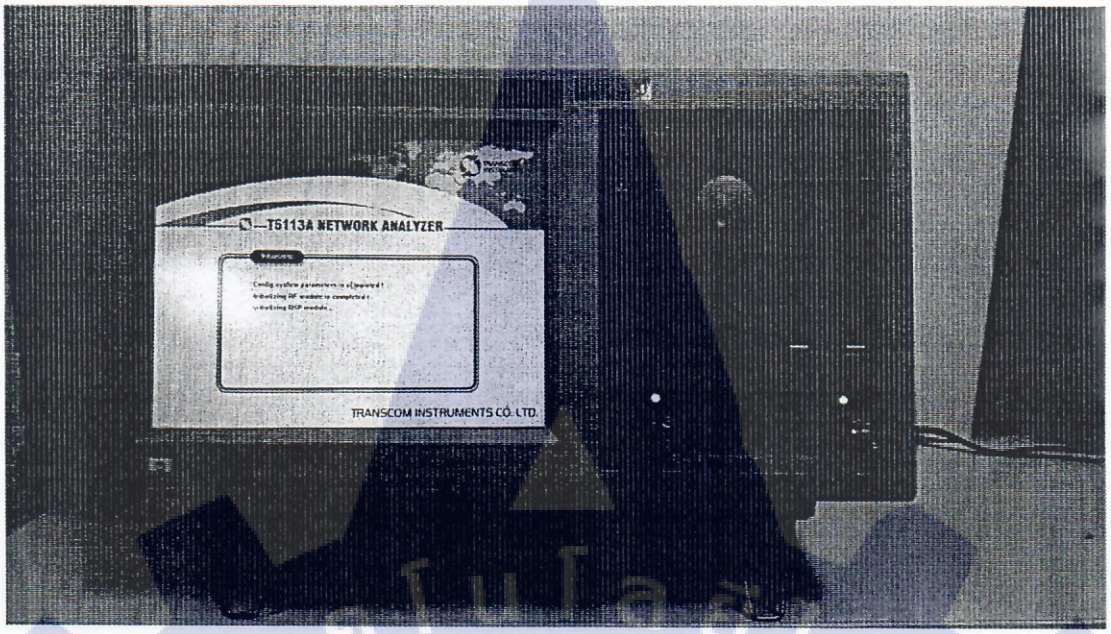

Figure 2.8: Network Analyzer.

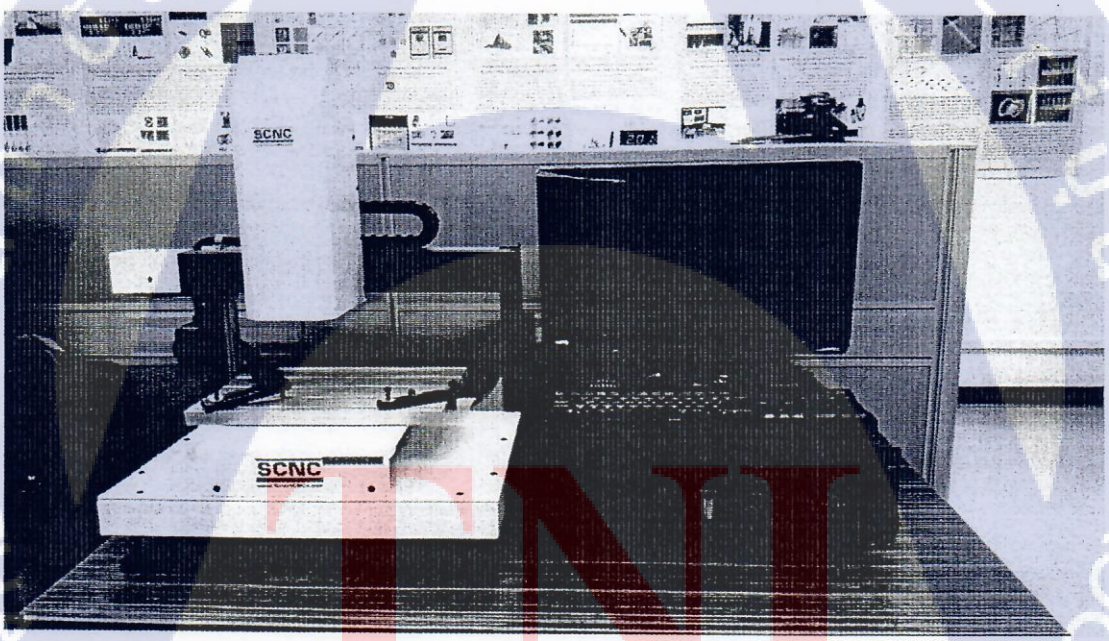

Figure 2.9 : Mini CNC Station.

3. Research on Intelligent Acoustic Emission

3.1 The Monitoring of 3DPrinter Filament Feeding Process

Additive manufacturing is a process which fabricate 3D object from CAD file by adding layers of material over another layer instead of subtracting material from material stock as in traditional process. This technique is becoming more popular in the present due to its numerous advantages such as increasing freedom in designing complex part, light weight product, and reducing material wastage. There are many sub techniques of this manufacturing procedure which are applied to manufacturing different type of materials [1]. However, there are still challenges such as improving materials and increasing the reliability and accuracy of equipment and processes [2] which are obstructing these techniques from being more widely used. In particular, quality of the process has been the challenges of such technology for a long time. In 1998, T. Fang et al. used image analyzing in attempt to monitor layered manufacturing of ceramics. The results showed an ability to detect defects in linear region. Nonetheless, there were some struggle with the end region which was not linear [3]. Recently in 2014, H. Rieder et al. applied ultrasonic which is one type of Non Destructive Testing (NDT) to selective laser melting technique which was used to manufacture products from metal powder. The fusion of a single layer and a temporal formation of material defects can be infer from such analysis [4].

However, in the field of fused filament deposited manufacturing of plastic, the fault detection is not as widely studied. J. Yoon et al. used heterodyne technique to lower sampling rate of Acoustic Emission sensor in order to compare the result with piezoelectric strain sensor. The aim was to detect driving belt seeded looseness fault where narrow band filter around high peak in frequency domain was used to extract condition indicators to detect the fault [5].

Nonetheless, there are still other problems with such type of process to be studied. One of the problems that could occur to the machine during the printing process is filament stop feeding through extruder [6]. This could be due to many causes such as level of build plate or clog in extruder. This problem could cause energy wastage or even lead to machine damage. Although it can be spotted by a cautious observer, in a long period work, the

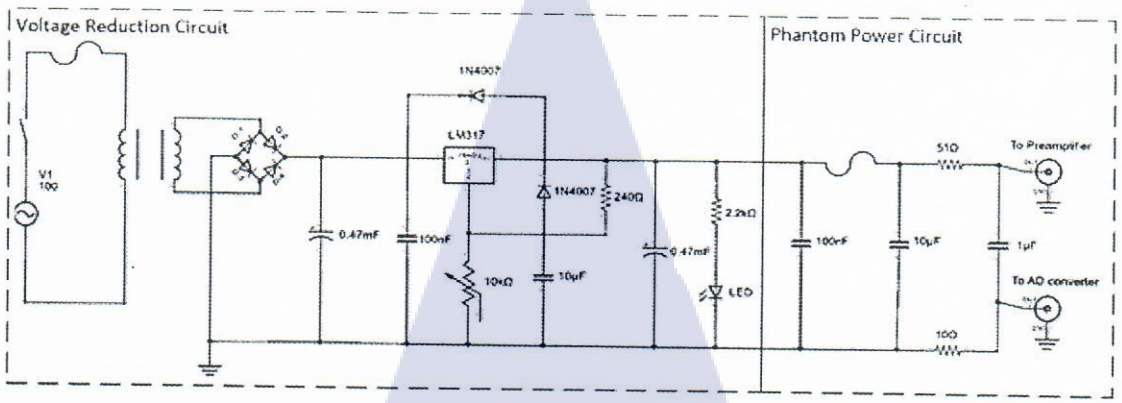

Figure 10 : Schematic diagram of low-cost power supply circuit.

process is usually run without an observer. A user could end up spending hours of processing time but receiving nothing but a piece of scrap and wastage of time and energy.

Acoustic Emission is one of Non Destruction Test (NDT) methods which allow specimen monitoring during the process without having to destroy it. AE is utilized in many conditions monitoring including many rotating and reciprocating machinery applications [7]. It has advantage of early detection due to its sensitivity [8]. It is also non-directional which give ability to detect the whole machine with only one sensor instead of multiple sensors for multiple directions.

In addition, Fast Fourier Transform (FFT) and frequency-domain analysis are commonly used in combining with AE to analyze and interpret such signal. FFT is a tool to convert time-domain signal to frequency-domain signal. It is useful in condition monitoring and fault prognosis which fault usually occurs in different frequency band from usual working frequency band.

This work presents an alternative to monitor filament feeding process in fused deposition additive manufacturing using an Acoustic Emission sensor. Low cost power supply and 3D-printed magnetic mounting are also equipped in the system for cost reduction and fine signal transmission. The signals are processed using Labview program in which Fast Fourier Transform and frequency-domain analysis are used as tools for the analysis. Finally, the comparison between normal and faulty machine is presented as a result.

The proposed monitoring system makes it possible to build a system to inform the operator about the operating status and possible to reduce the loss of time and energy which is considered to lead to EcoDesign.

Prior to the experiment, the AE system was assembled by combining the essential instruments. Despite preparation of commercial parts for the study, some parts were fabricated to suit the requirement of this particular experiment in low cost. These parts are power supply and sensor mounting.

3.1.1 Low Cost Power Supply

In order to complete the system, a pre-amplifier was required to be connected to a power supply which also serves as a terminal to transfer signal to Analog-to-Digital (A/D) converter. Therefore, a power supply was fabricated using voltage reduction circuit to utilize 100V-AC household electricity. The objective is to fabricate low cost power supply that could perform as a commercial power supply for AE sensor.

The power supply circuit consists of 2 main parts which are the voltage reduction circuit and the phantom power circuit which is the circuit to connect power supply with preamplifier and to acquire output signal. The schematic diagram of both parts of the circuit is shown in Fig. 3.1. The first part or the voltage reduction circuit used transformer to reduce 100 V-AC household electricity to 50 V-AC. Then, Diode Bridge was utilized to convert AC electricity to DC electricity. After that, LM317 adjustable voltage regulator was employed to adjust the output voltage to the desired voltage. This was achieved by potentiometer usage. The output voltage can be calculated from the following formula [9];

$$V_o = V_{ref} \times \left(1 + \frac{R_2}{R_1}\right) + I_{adj}R_2 \qquad (3.1)$$

where is an output voltage, is an input voltage to LM317, is a resistance of potentiometer, is a resistance of 240 Ohm resistor, and is the current of the adjust pin. However, the device, LM317, was designed to minimize current of the adjust pin. Therefore, the term can be neglected and the formula can be rewritten as;

$$V_o = V_{ref} \times \left(1 + \frac{R}{240}\right) \qquad (3.2)$$

In addition, the performance and the stability of the circuit are enhanced by utilizing several diodes and capacitors. Diodes are utilized in order to

prevent misdirection electrical while capacitors are utilized in order to stabilize electrical level in the circuit.

The second part of the circuit or the phantom power circuit was adopted from the manufacturer's website. The objective of this part of circuit is for the sensor and the preamplifier share an AE output signal and a preamplifier power within a single cable [10]. BNC connectors were employed as a low-noise connection platform. An LED lamp and switch were also utilized to fulfill the power supply as an indicator and a control of power supply status, respectively. The completely fabricated power supply, both inside circuit and outside apparatus, is shown in Fig. 3.2, (a) and (b) respectively.

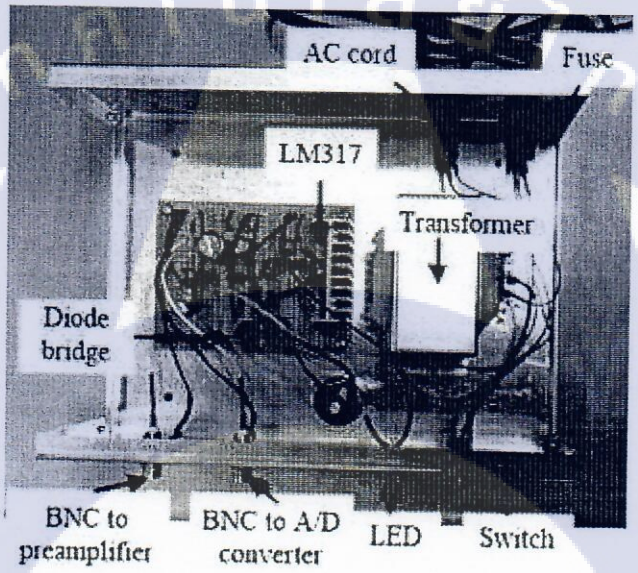

(a)

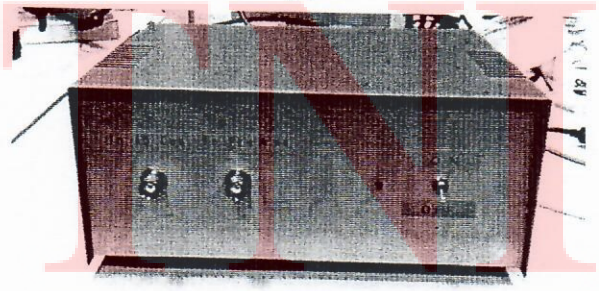

(b)

Figure 11: (a) Inside circuit and (b) apparatus of the fabricated power supply

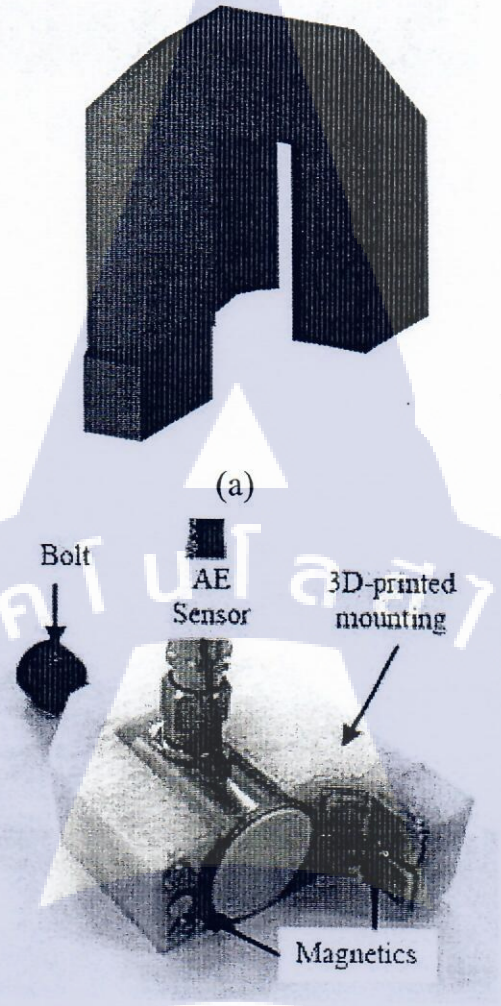

Figure 12: (a) CAD prototype and (b) final assembly of AE sensor and magnetic mounting

3.1.2 3D-Printed Magnetic Mounting

Attaching AE sensor to the testing machine was another consideration point. Well attachment would assure fine signal transmission which prevents detail loss in the process. Sensor coupling is an agent to substitute air between surface of the sensor and surface of the machine. Among different types of coupling, grease-based coupling have high viscosity which is suitable for rough surface and long-term stability. It also has ability to withstand medium temperature [11]. This is appropriate for the application with 3D printer which has rough surface and vibration during the working process. Therefore, vacuum silicone grease was chosen as a sensor coupling in this study.

In order to use grease as sensor coupling, clamp was required. However, the dimension of the 3D printer motor block caused commercial mountings to be not so applicable. Therefore, AE sensor mounting was design using CAD software to perfectly match the dimension of the motor block. The rendering of CAD file of the mounting is shown in Fig. 3.4(a) and can be downloaded at [12]. Then, the mounting was fabricated using 3D printer which gave freedom in designing and also low cost product. After that magnets and a bolt were assembled to the printed object to complete the fabrication as shown in Fig. 3.4b. The screw bolt was utilized in the design to help securing the sensor and benefits in removing trapped air between surfaces.

In addition, AE sensor is attach to motor block using double-sided tape as a simple connecting agent and collect data for normal working condition to test the effectiveness of magnetic mounting and vacuum grease as pre-conditioned experiment. This is to use as a reference data to compare with tested data in the main experiment.

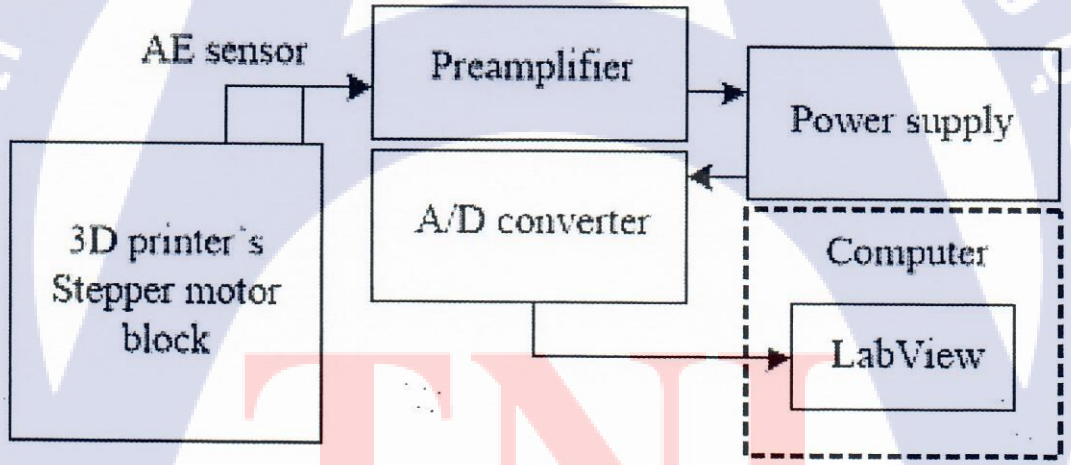

Figure 13 : Signal flow of the test system.

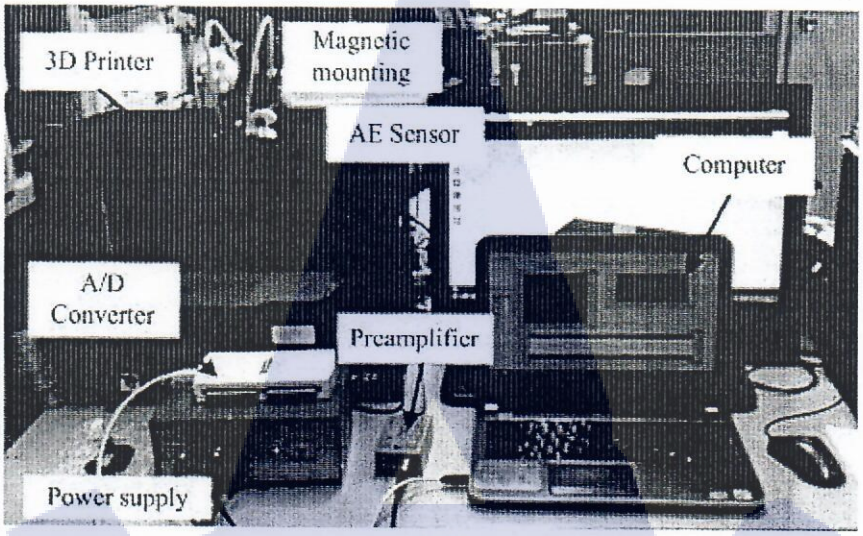

Figure 14: Apparatus of the test rig.

An overview of the test is shown in block diagram in Fig 4 with arrows which show the flow of the signal through the test system. The test rig consisted of a 3D printer, an AE sensor, a preamplifier, a fabricated power supply, an A/D converter, and a computer. An AE sensor was attached to the extruder's stepper motor of the 3D printer using a 3D-printed magnetic mounting which was fabricated in section 2A with silicone vacuum grease applied between AE sensor and stepper motor surfaces. The signal was collected from the stepper motor using AE sensor. Then, the signal was transmitted to the preamplifier with 60-dB gain to amplify the amplitude and the detail of the signal. After that, the signal was collected through an A/D converter and then analyzed using LabView program using FFT procedure, respectively. The experimental apparatus is shown in Fig. 3.5.

3.1.3 Attachment comparison experiment

Prior to the main experiment, pre-conditioned experiment was performed to discover the appropriate attachment methodology to be applied for the main experiment of this study. Two attachment methodologies which would be tested in this study were a double-sided tape and a fabricated magnetic mounting with vacuum silicone grease. Double-sided tape attachment is a simple attachment which allow strong bond between AE sensor and the specimen. It can be easily applied without any other components and can be attached to many different surfaces both vertical and horizontal. On the other hand, 3D-printed magnetic mounting and vacuum silicone grease were designed to suit this particular dimension of the motor block.

Both methods were applied to attach an AE sensor to the stepper motor of 3D printer then signals were acquired from normally working conditioned 3D printer. After that, these signals would be compared by mainly focusing on the amplitude and details of the signal. Effectiveness of both attachment methodologies would be compared in order to discover more suitable methodologies for the main experiment to assure well signal transmission for further analysis. Experiment setup for both attachment methodologies are shown Fig 3.6, (a) for double-sided tape and (b) for fabricated magnetic mounting.

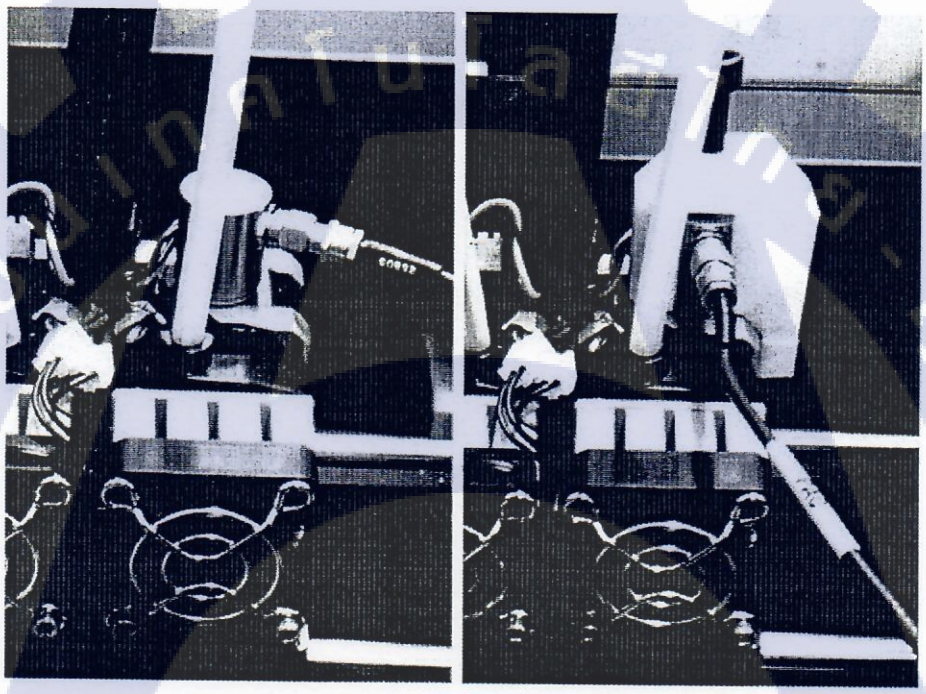

(a) (b)

Figure 15 : (a) Double-sided tape and (b) fabricated magnetic mounting experiment setup for an attachment comparison.

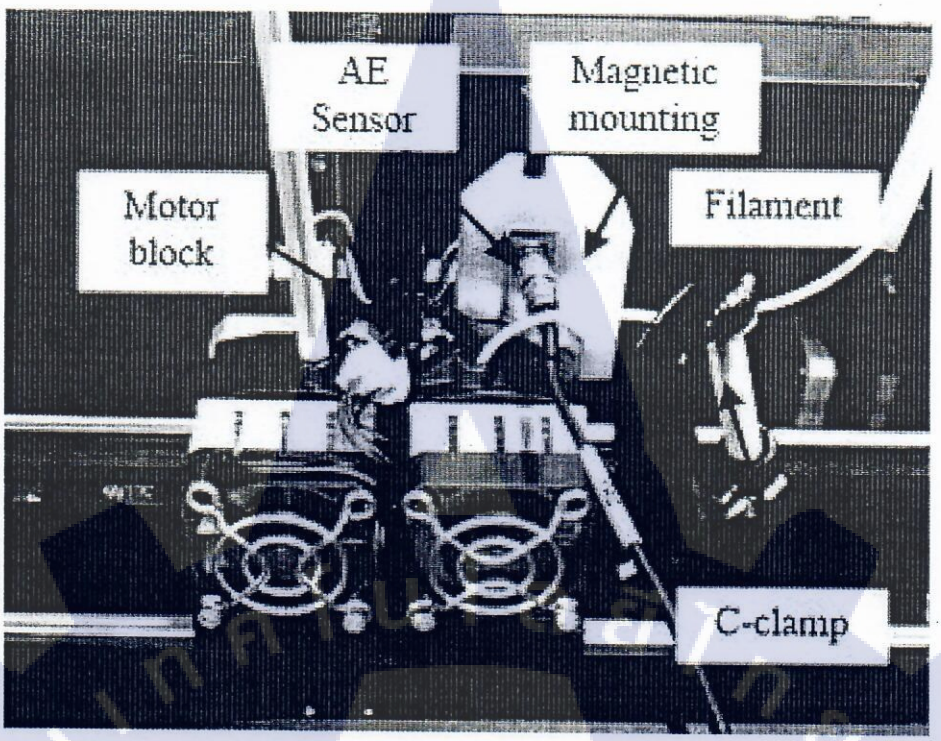

Figure 16 : Setup of filament feeding condition experiment.

3.1.4 Filament feeding condition experiment

The main experiment of this study was the study of AE signals under different conditions of 3D printer. The experiment consisted of 3 conditions which were filament normally feeding condition, filament stop feeding through the extruder condition, and no filament supply for the extruder condition.

For the first condition, an AE sensor was attached to a properly working 3D printer to acquire signals as a reference signal. For the second condition which is filament stop feeding condition, in order to simulate filament stop feeding through the extruder, a C-clamp was attached to the filament, which was feeding to the extruder, in order to block the filament from feeding into the extruder. The components and setup of such experimental condition is shown in Fig 3.6. The signal would be collected after C-clamp has settled on the top of the extruder and the filament has been perfectly stopped.

For the last condition, the no filament condition, filament was unloaded from the extruder using unload function of the printer. The printer was tested to assure that there is no filament going through the extruder

before the signal would be collected. The experimental setup of such condition is shown in Fig 3.7.

The signals of each condition were collected separately and analyzed using LabView program. The analyzing program consisted of time-domain signal, frequency-domain signal acquiring from Fast Fourier Transform, and frequency and its value of peak amplitudes. The data from each condition was then compared in order to discover the distinguish parameter in the last step.

3.1.5 Result and Discussion

3.1.5.1 Result of attachment comparison experiment

The time-domain signal of a normally working 3D printer using double-sided tape as an attachment of an AE sensor is shown in Fig. 9 while the time-domain signal of a normally working 3D printer using a magnetic mounting and vacuum silicone grease as an AE sensor coupling is shown in Fig. 10. Comparing both figures, difference in amplitudes can be noticed that amplitude of the signal in Fig. 10 is about 3 times larger than in Fig. 9. This shows ability of a magnetic mounting and vacuum grease as a coupling to attach AE sensor to the motor block. As a result of this pre-conditioned experiment, the magnetic mounting and vacuum grease was continually utilized as sensor coupling in the main experiment.

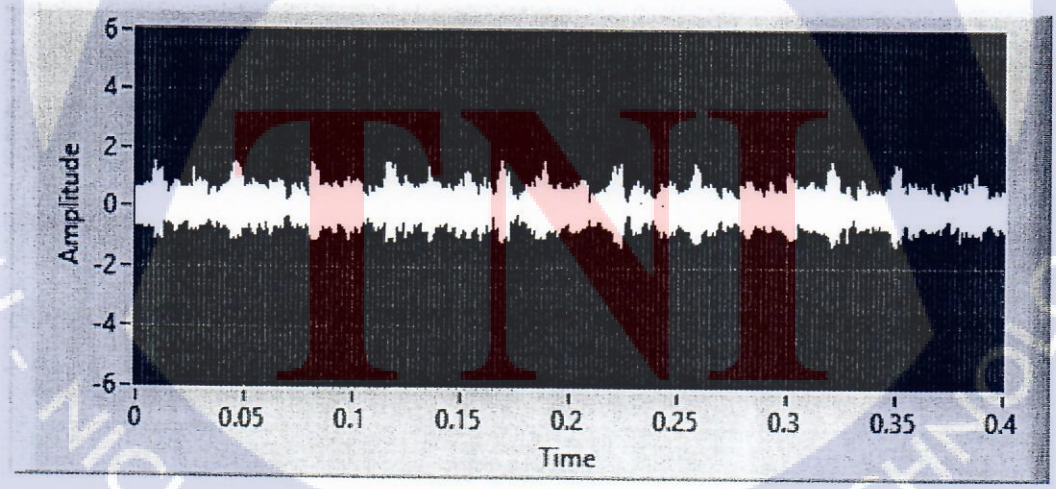

Figure 17: Time-domain signal of normal condition using double-sided tape as an attachment.

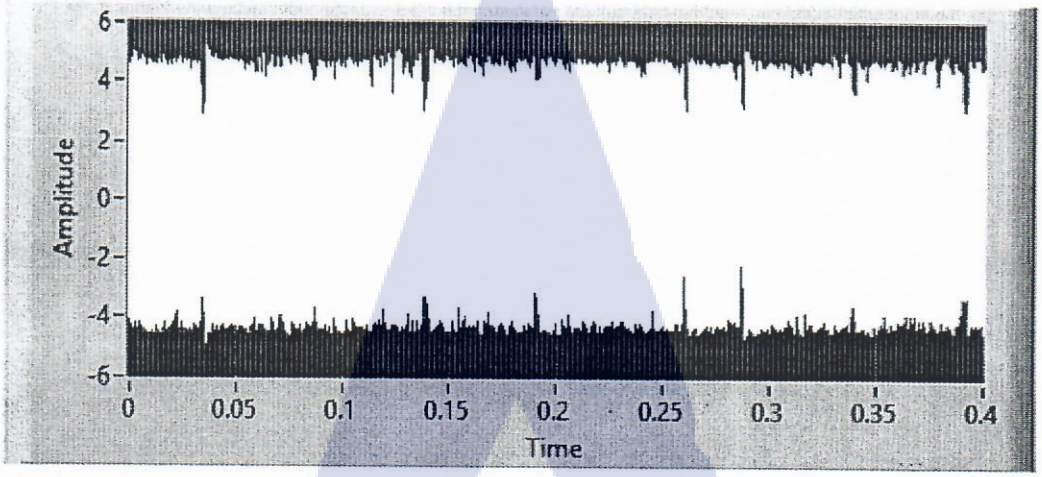

Figure 18: Time-domain signal of normal condition using magnetic mounting and vacuum grease.

3.1.5.2 Result of filament feeding experiment

The time-domain signal for filament stop feeding condition is shown in Fig. 3.8. Comparing to the signal in normal condition in Fig. 3.9, these signals show very similar characteristics which is difficult to distinguish faulty condition of the machine.

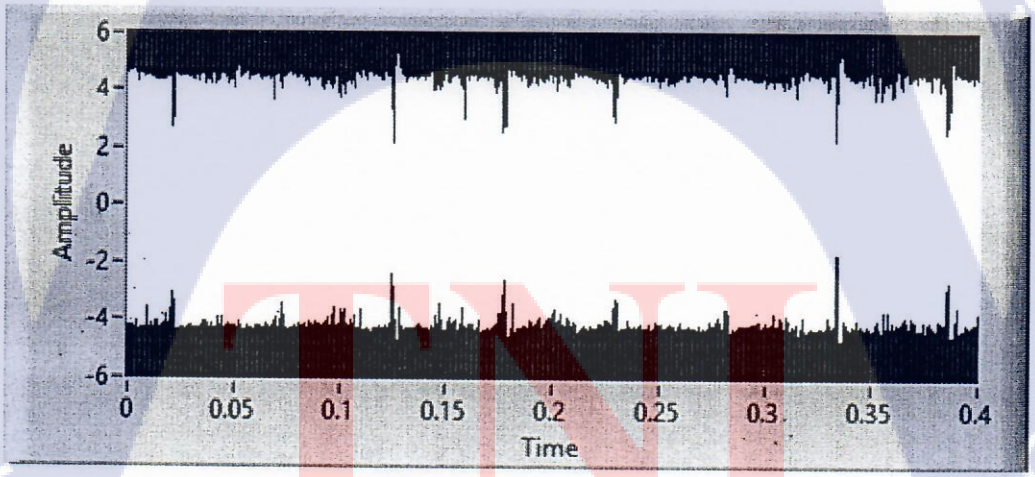

Figure 19 : Time-domain signal of filament stop feeding condition.

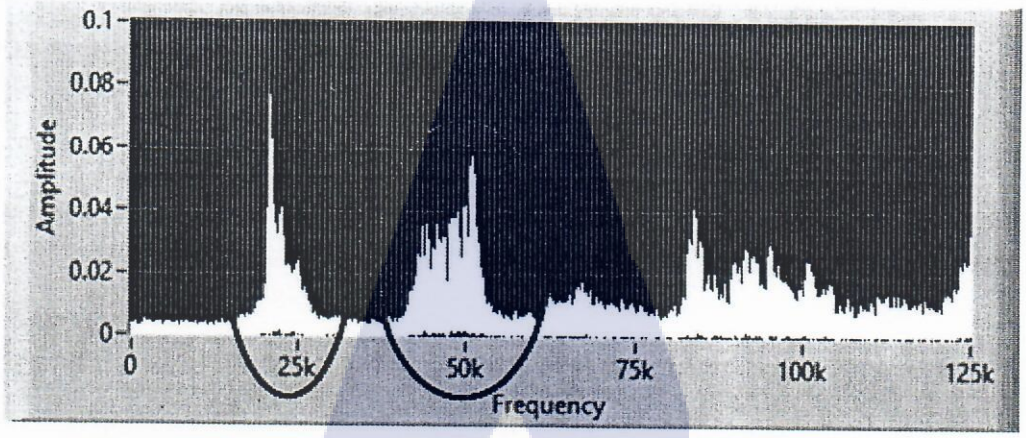

Figure 20: Frequency-domain signal of normal condition.

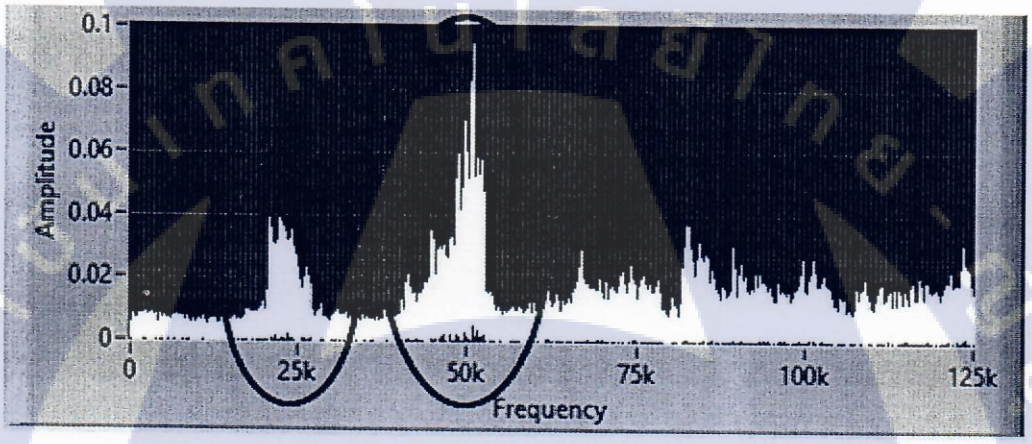

Figure 21 : Frequency-domain signal of filament stop feeding condition.

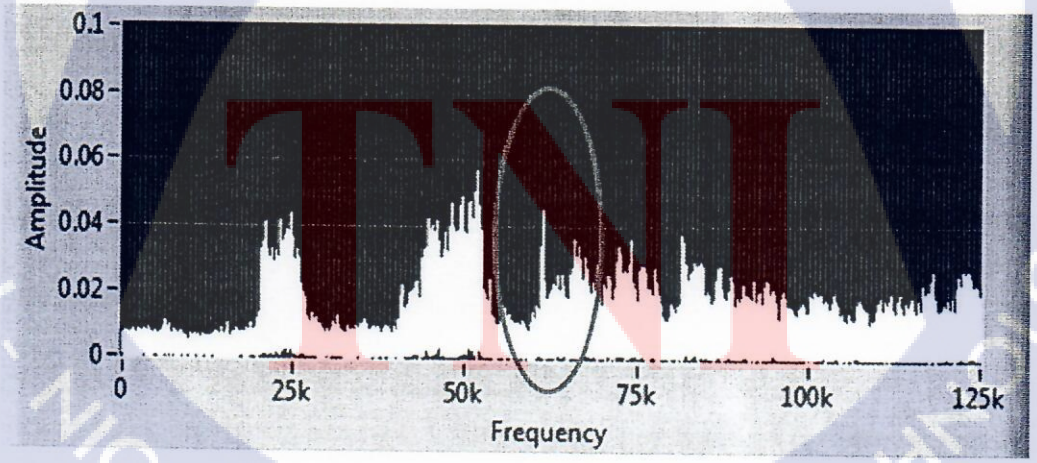

Figure 22 : Frequency-domain signal of no filament feeding condition.

Therefore, the Fast Fourier Transform was utilized and frequency-domain signal was acquired as shown in Fig. 3.11 and Fig. 3.12 for normal condition and filament stop feeding condition, respectively. Different in frequency of maximum amplitude of the signal can be clearly noticed. Although high amplitude around 20 kHz and 50 kHz can be noticed from both conditions, normal condition has its maximum amplitude in 20kHz frequency band while filament stop feeding condition has its maximum amplitude in 50kHz frequency band. In the other word, for normal condition, amplitude of 20 kHz frequency band is higher than in filament stop feeding condition while for 50 kHz band, signal from filament stop feeding condition shows higher amplitude than normal condition. Consequently, it can be assumed that 50 kHz frequency band is the frequency of working motor while the peak at 20 kHz band is caused by the process of filament feeding through the extruder.

In addition, frequency-domain signal of no filament feeding condition is shown in Fig 3.13. Comparing filament stop feeding and no filament feeding condition, both conditions show maximum amplitude at 50 kHz frequency band. This is consistent with the previous conclusion since no filament feeing condition can be considered in the same category as filament stop feeding because both conditions result in no filament through the extruder. However, the causes were different, blockage for filament stop feeding condition and lack of filament for no filament condition. Methodologies to resolve the problems were consequently different.

Realizing such information, further comparison of both conditions were performed by a scatter plotted in Fig 3.14. This plot support the observation in Fig 3.14 that when there is no filament supplying for the extruder, there would be an additional peak around 60 kHz frequency band. Therefore, no filament feeding condition can be distinguished from filament stop feeding by using this frequency band.

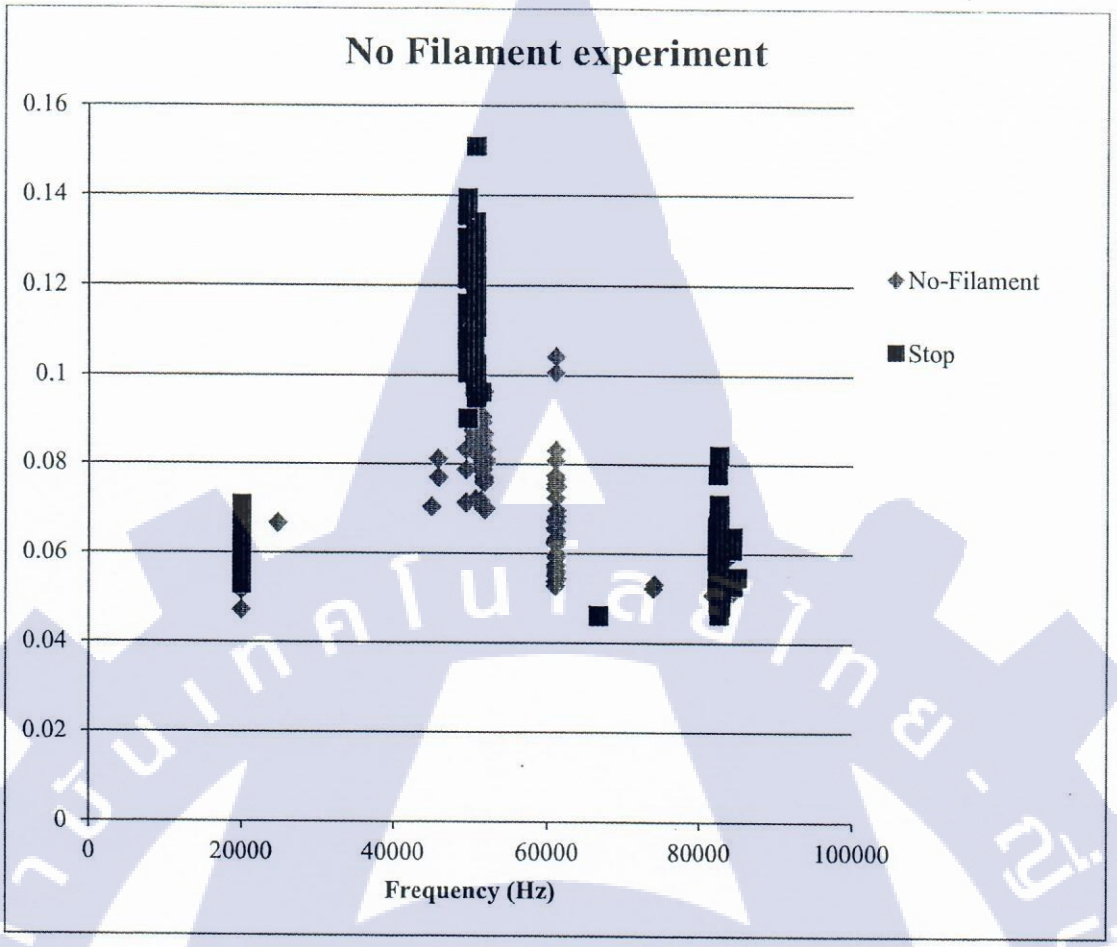

Figure 23: Frequency-domain signal of no filament feeding condition

3.1.6 Conclusion

Acoustic Emission sensor has been utilized to monitor the process of filament feeding in a filament deposit 3D-printer which is one type of an Additive Manufacturing. Low cost power supply and 3D-printed magnetic mounting was also equipped to acquire effective signal collecting system in low cost. The signal was processed using Fast Fourier transform and frequency-domain analysis through LabView program. The result shows noticeable different between normally operating machine and machine with filament feeding problem including filament stop feeding condition and no filament feeding condition using frequency of maximum amplitude and amplitude of peaks of the signal as a distinguish tool. An ability of AE sensor in monitoring 3D printer is demonstrated.

3.2 A Low-Cost Microcontroller-Based Data Acquisition System for Acoustic Emission Sensors

3.2.1 Introduction

Machine condition monitoring and fault diagnosis systems are essential tools for the non-destructive testing and maintenance. Input signals in such systems are generally generated by a variety of sensors and transducers that measure temperature, pressure, vibration, and particularly Acoustic Emission (AE) signals [13]. The acoustic emission signal is typically a sound wave generated when a material undergoes stress due to external forces. The AE signal is a phenomenon occurring in, for instance, mechanical loading generating sources of elastic waves. Such occurrences are the results of a slight surface displacement of materials produced from stress waves, which is generated when the energy in materials or on its surface is released rapidly [14].

In order to detect such AE signals for the purpose of monitoring or maintenance, Data Acquisition (DAQ) system, i.e. a process of measuring an electrical or physical phenomenon, is necessarily and ultimately required to display the signal in computer for further signal condition analysis. Fig.3.15 shows general perspectives on a typical and the proposed AE signal detection systems using low-cost

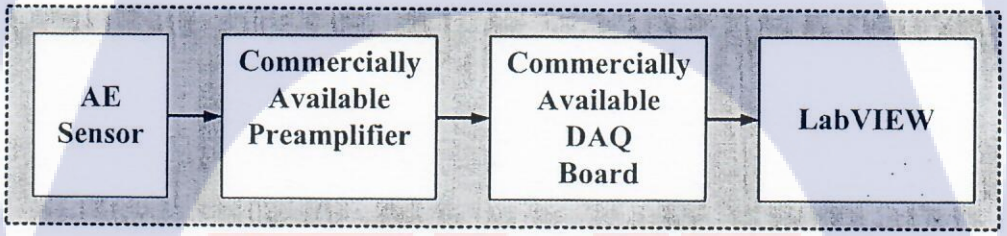

(a) Commercially Available AE Signal Detection

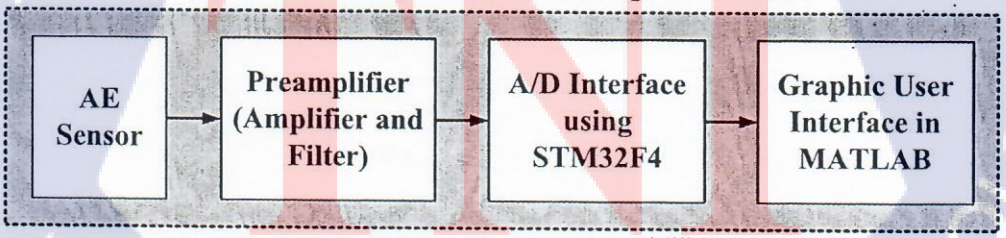

(b) Research Focus for the Low-Cost DAQ System for AE Signal Detection

Figure 24 : General perspective on (a) a typical and (b) the proposed AE signal detection systems using low-cost preamplifier and STM32F4 Microcontroller.

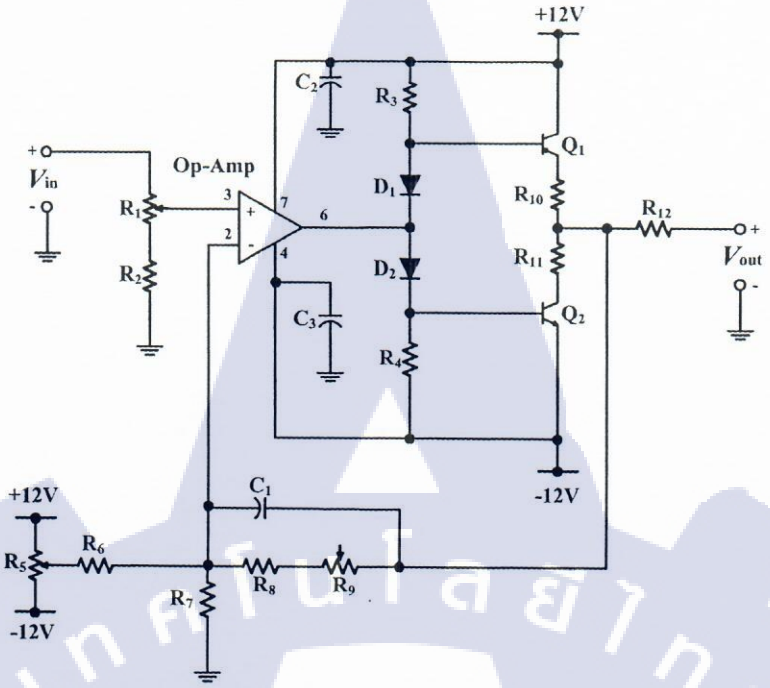

(a)

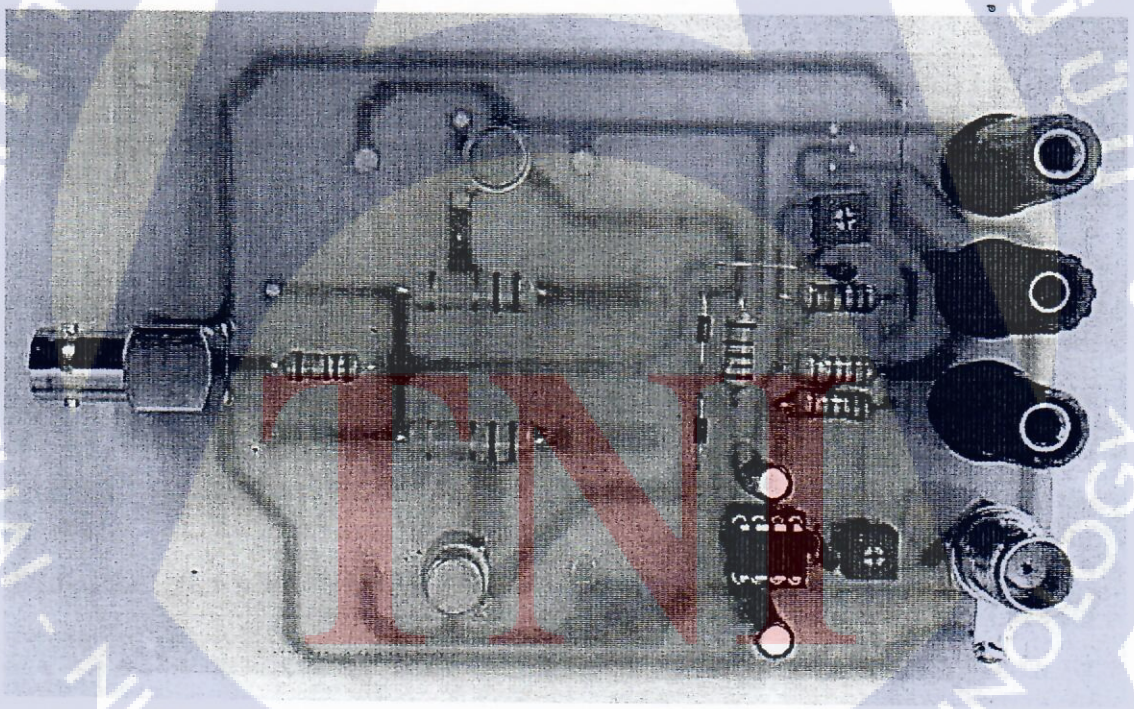

(b)

Figure 25: The preamplfier circuit designs; (a) circuit schematic diagram, (b) circuit implementation on board.

preamplifier and STM32F4 microcontroller. It can be seen in Fig.3.15 (a) that most typical AE signal detection employ DAQ board with high speed data transmission and utilize LabVIEW program that readily provide some fundamental analysis methods such as Fast Fourier Transform in a frequency domain [15,16]. Such systems are relatively complicated as numerous devices are required. Typically, the DAQ system consists of sensor input, measurement hardware, and a computer with licensed programmable software. Despite the fact that such commercially available DAQ system exploits the processing power, productivity, and connectivity capabilities of industry-standard computers with high effectiveness, the price is relatively costly and may not be suitable for some low-frequency applications, especially Small and Medium Enterprises (SME).

In Fig.3.15 (b), this work, however, alternatively focuses on the possibility of implementing a low-cost preamplifier and DAQ system through the use of STM32F4 Microcontroller for transmitting AE signal data to MATLAB analysis software via serial communication. Although there has been numerous research reports for AE signal feature characterizations that include commercially available DAQ system [17-22], no particular research interests has been reported relating a simple-but-robust DAQ system especially with having low-cost capability for SMEs in Thailand.

The overall system designs in this research focuses on cost-effective DAQ board and signal analysis in the frequency domain. The proposed system consists of three major blocks. First, an integrated amplifier and filter so called "preamplifier" employed in order to amplify the receiving input AE signal with variable gains and filtering noises in environments. Second, the use of analog-to-digital conversion system in the STM32F4 microcontroller with real-time operation. In addition, such a STM32F4 microcontroller has an ability of connecting directly to computer with MATLAB program interface. Last, the Graphic User Interface (GUI) that exploits MATLAB program to display real-time AE signals and various signal characteristics analysis. In this work, the AE signal is initially considered as a sinusoidal signal, which represents the AE signal at single harmonic amplitude, for analyzing the DAQ characteristics. The real AE signals receiving from AE sensors are also demonstrated ultimately.

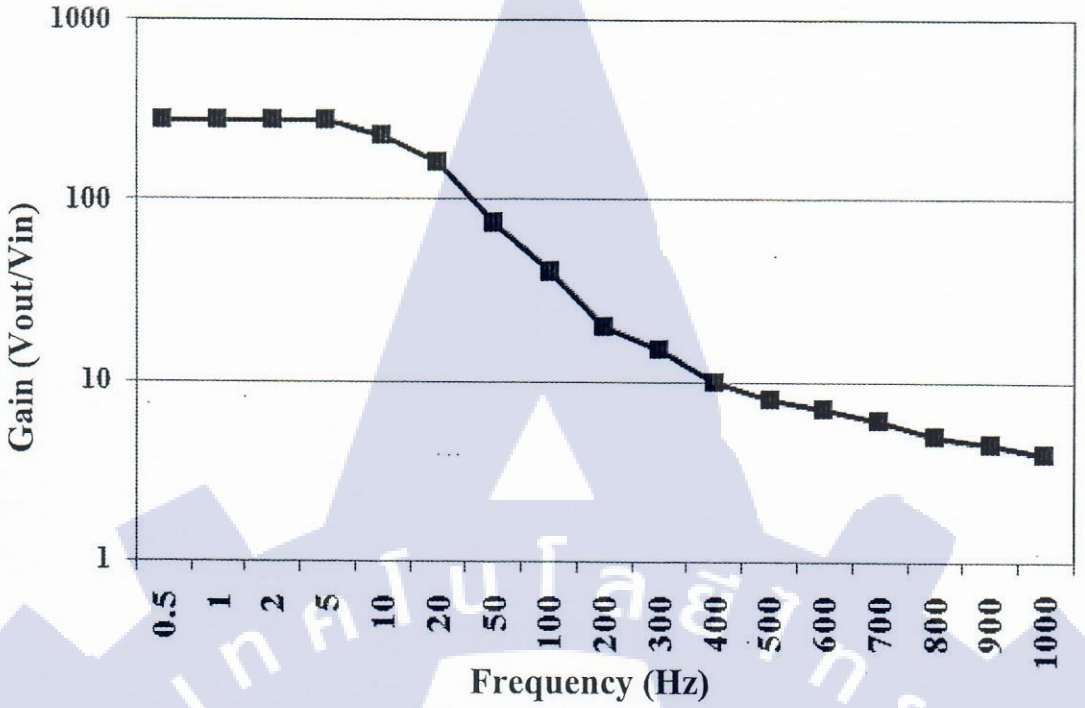

Figure 26: Frequency response characteristics of the proposed preamplifier.

3.2.2 Preamplifier Circuit Designs

Figs. 3.16 (a) and (b) show the preamplifier circuit designs. The variable gain preamplifier is implemented using BiMOS operational amplifier model CA3140 as a high slew rate, wideband amplifier. The amplifier circuit has been designed based on a non-inverting amplifier which analog input signal is connected at the input terminal which signal level can be adjusted by R1 before input of CA3140. Gain of preamplifier can be adjusted via R9 and output DC level can also be adjusted by R5 to keep output signal at the output terminal in the range of 0-3 V that compatible with STM32F4 Controller. The push-pull class AB output circuit using transistors Q1 (2N3053) and Q2 (2N4037) are exploited in order to adjust full peak-to-peak swing. Values of electrical components are listed as follows; R1=2kΩ, R2=200Ω, R3=2.2kΩ, R4=2.2kΩ, R5=10kΩ, R6=3kΩ, R7=200Ω, R8=2.2kΩ, R9=50kΩ, R10=2.7Ω, R11=2.7Ω, R12=51Ω, C1=2pF, C2=50μF, C3=50μF, and the diode model is 1N914. Fig.3 shows the frequency response characteristics of the preamplifier in linear gain scale. It can be seen from the graph that the preamplifier establish the low pass filter characteristic where the low frequency has a very high gain of above 100 but at the high frequency, for example 1 MHz, the gain is still

greater than 0. For the frequency of interest at 100 kHz the gain is approximately at 20dB.

3.2.3 STM32F4 Microcontroller Interface Operations

As mentioned earlier, this work utilizes the STM32F4 controller, which is based on the high-performance ARM®Cortex™-M4 32-bit RISC core operating at a frequency of up to 168 MHz, for analog-to-digital conversion. This device offers three 12-bit ADCs, two DACs, a low-power RTC, twelve general-purpose 16-bit timers including two PWM timers for motor control, two general-purpose 32-bit timers. Therefore, the input analog signal is digitized with the performance of 3×12-BIT AMD 2.4 MSPS.

3.2.4 Standard Tests for AE Signal Detections

The commercially available AE sensor was calibrated using the standard pencil lead break tests on an aluminum plate according to the artificial source, i.e. ASTM Standard No. E976-84 [11]. The commercial preamplifier with three selectable different gains at 20dB, 40dB and 60dB were exploits for investigating the magnitudes and the number of counts based on different threshold voltage. As for instance in the case of the standard AE signal tests and calibrations at 60dB amplification, Figs.3.18 (a) and (b) shows the waveforms of the detected AE signals in time domain and the corresponding power spectral density in dB, respectively. Both graphs are obtained from LabVIEW.

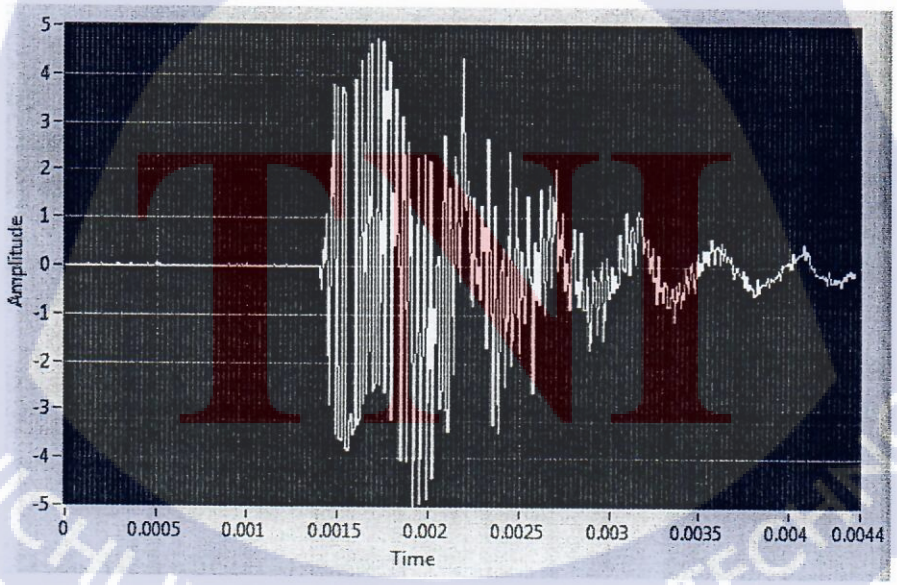

(a) Detected waveforms of AE signals.

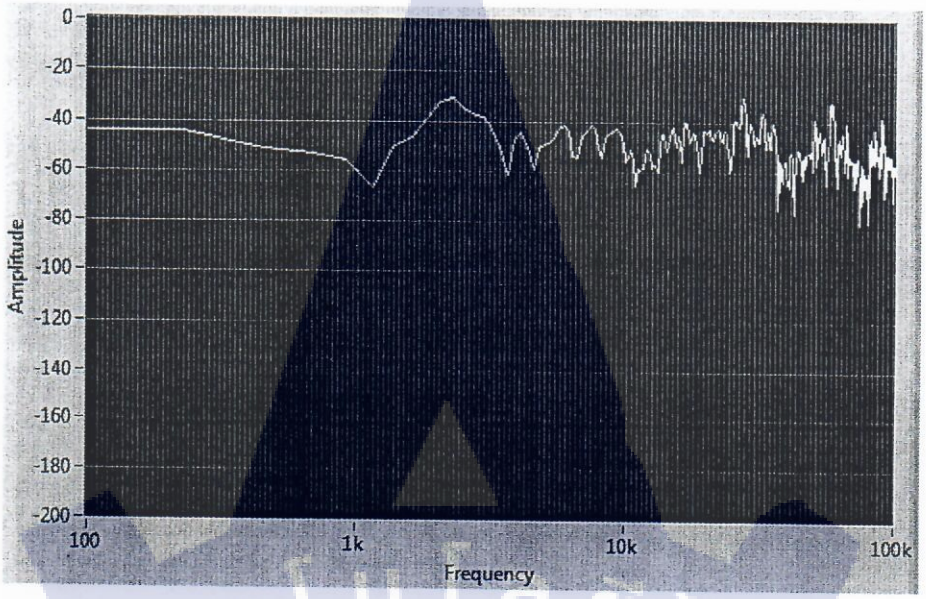

(b) Power spectral density in dB.

Figure 27 : Results of standard AE signal tests and calibrations at 60dB amplification in LabVIEW; (a) Waveformes of the detected AE signals, (b) the corresponding power spectral density in dB.

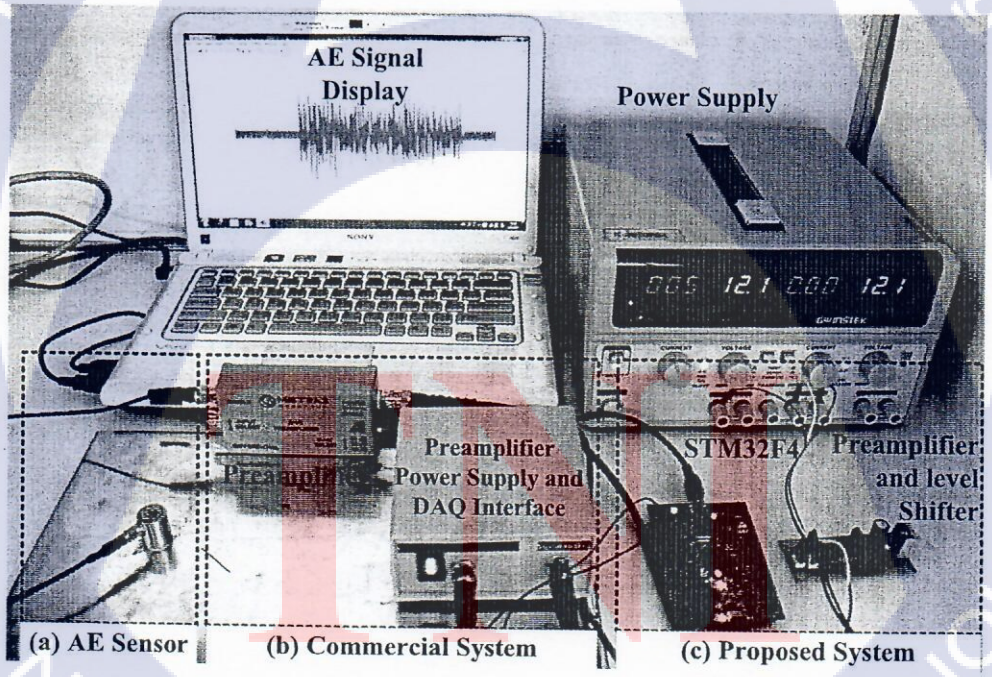

Figure 28 : Experimental apparatus of (a) a typical and (b) the proposed AE signal detection systems using low-cost preamplifier and STM32F4 Microcontroller.

Table 3.1.

Summary of Particular Gains (v_{out}/v_{in}) And Showing the Corresponding THD in Percentages

Particular Gains	THD (%)
5	3.2362
10	3.7334
15	5.4146
20	5.6488

3.2.5 Experimental Results

The experimental results have been performed through the protoboard corresponding to the block diagram in Figs.3.19 (a) and (b) as illustrated in Fig.3.18. Initially, the demonstration condition is a sinusoidal signal input of 20mV at 100 kHz. Fig. 3.19 illustrates the results of STM32F4 and the graphic user interface; (a) the power spectral density showing the bandwidth of the signal at dB level, (b) the display of signal in time and frequency domains from MATLAB. Using the rectangular window transformation, the peak signal at 100 kHz has the highest peak where the noise floor is about 200 kHz far from the center frequency. Since FFT transformation was used for the THD calculation, Table 3.1 summarized the THD in percentage at difference value of particular linear gain under region of interest between 5-20. It is seen that the THD is in the range of 3-5%. This is acceptable for the preamplifier

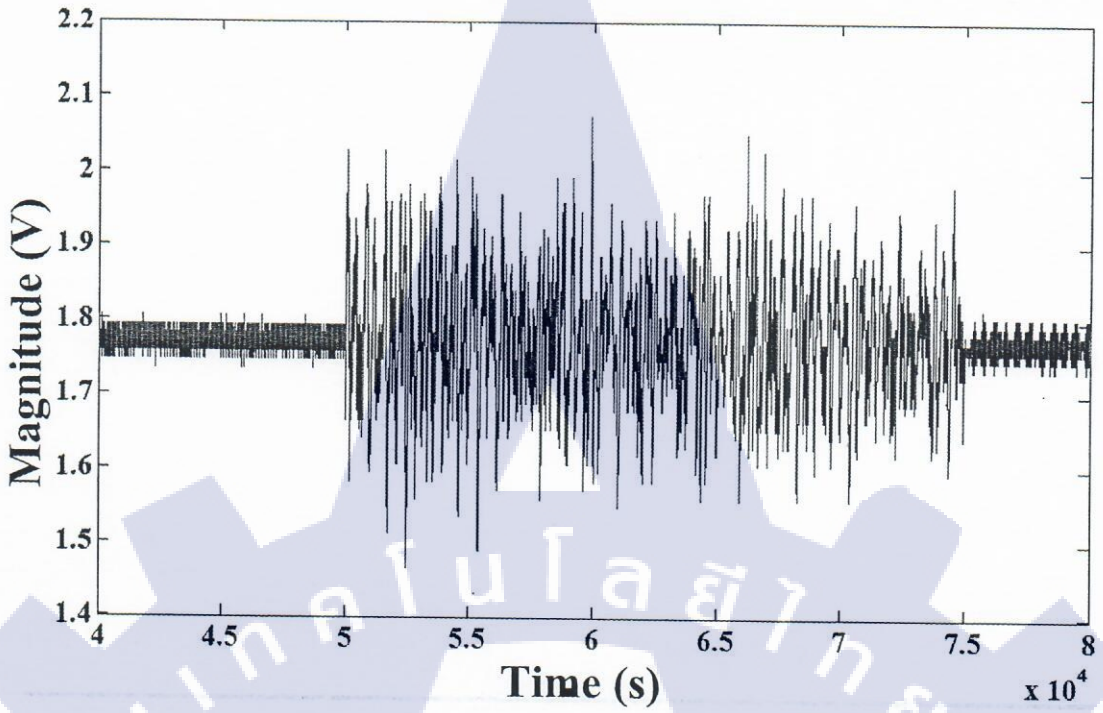

Figure 29 Results of the proposed systen that detects the AE signals in time domain.

that amplifies the AE signal in real application. Fig.7 shows the results of the proposed system that detects the AE signals in time domain. It is seen in Fig.7 that the use of low-cost preamplifier and STM32F4 microcontroller can also potentially detect the input AE signals.

3.2.6 Conclusions

This work has presented the data acquisition system that particularly collects AE signals in the range of 1 kHz to 100 kHz from the sensor, and transmits to a personal computer for further signal analyses. The proposed system comprises three major components, i.e. a variable gain preamplifier and a STM32F4 Microcontroller, and a graphic user interface (GUI). The variable gain preamplifier is implemented using BiMOS operational amplifier model CA3140 which provides relatively high input impedance and high-speed performance. It is obviously seen through the results that the quality signal analysis were strongly satisfy including high frequency response at high voltage gain, obtain the peak of signal at 100 kHz. The generated signal was successfully digitized by STM32F4 Microcontroller and transmits to a MATLAB Simulink via serial communication (RS232). In addition, the proposed system offers a potential alternative cost-effective

data acquisition to commercially available data acquisition systems in the same range of frequency response such as National Instrument (NI), Physical Acoustics Corporation (PAC) etc. in which the cost could be reduced to approximately 20% comparing to the specified DAQs.

3.3 A Low-Cost Air Leakage Monitoring Technique for Industrial Compressed Air Piping Systems using Acoustic Emission Sensor

3.3.1 Introduction

A compressed air piping system has been utilized in a variety of commercial industrial facilities and considered as a utility essential to production. Applications are hand tools, air hammers, paving breakers, rock drills, positive displacement, pumps, paint chippers, air-actuated valves, and healthcare. The main purpose of using the compressed air piping system is to deliver compressed air to usage points with enough volume, appropriate quality, and pressure to properly power the components [23]. The compressed air piping system should be designed properly in order to achieve expected production efficiencies otherwise equipment failure and high energy costs may be occurred. In particular, time-dependent aging and instantaneous threats may result in pipeline damage that propagates through structural thickness and causes air leakage. Therefore, an early detection of leakage in pipeline networks is essential to prevent any catastrophic failures. The leak in pressurized pipelines generally causes turbulent flow at its location, which generates solid particles or gas bubbles. The impact energy causes propagating elastic waves that can be detected by the sensors mounted on the pipeline [24].

Acoustic Emission (AE) is the generation of transient elastic waves that occurs when materials undergo deformation fracture leakage. In order to inspect such an AE phenomenon, pipeline leakage can be effectively detected by using an AE sensor [25]. Typically, the AE sensor is a piezoelectric transducer composed of special ceramic elements such as Lead Airconate Titivate (PZT). Mechanical strain of a piezoelectric element generates an electrical signal, which is an indispensable component used to collect information in AE inspection process. The AE sensing technique can be considered as one of Non-Destructive Inspection (NDI) methods that show its ability in monitoring air leakage of a steel pipeline.

The NDI method using the AE sensor is different from other NDI techniques in two approaches [26]. The first difference pertains to the origin

of the signal in a manner that instead of supplying energy to the object under inspection, the AE sensing technique is attend for the energy released by the object. The second difference is that the AE sensing technique deals with dynamic processes in materials, which is particularly important as only active features are investigated.

There has been various NDI using AE sensing techniques proposed for detecting and monitoring pipeline leakage. P. Davis and J. Brockhurst [27] presented leak detection in liquid filled buried pipeline using AE sensing technique that detects the turbulent flow at the leak orifice. In addition, the position of the leak is provided through the use of digital AE systems and specialized software. T. Kaewkongkal and J. Lim [28] studied the application of AE for pipeline condition monitoring using pre-processed AE parameter and Gaussian distribution to establish characteristic features relating to each pipeline condition. For AE analysis methods, R. Wu and et.al. [29] proposed wavelet transform in AE signal detection under strong noises, which is accurate and computationally implemental for embedded systems. Comparison between Short-Time Fourier Transform (STFT) and wavelet transforms were also made. Besides, L. Sun and et.al. [30] compares two non-destructive inspection methods for pressure pipes between Magnetic Flux Leakage (MFL) and AE techniques. Recently, D. Feng and et.al. [31] also suggested a leak-detection system suitable for liquid pipeline through the use of two sensors, i.e. AE and pressure sensors. S. L. Ying and et.al. [32] presented an adaptive leak detection and location scheme for gas pipelines by using AE sensors. Additionally, S. Li and et.al. [33] proposed comparison method using spectral for leak signal with different detection distance, revealing different features of leak signal at different pressure and leakage aperture.

This work presents the NDI of industrial compressed air piping system using AE sensing technique. The major objective is to implement a cost-effective AE sensing system for industrial applications where a single AE sensor is realized for signal characterizations through Fast-Fourier Transform (FFT) algorithm. Focusing on AE signal features in frequency domain as a tool, characteristics of a leakage detection system will be experimentally clarified through normal and faulty conditions.

3.3.2 Mathematical Models of AE Signals

The AE sensing techniques typically counts on a propagating transient wave generated by sudden stress-strain change in a material. According to the standard ASTME 1316 [34], the two categories of AE signals are (1) a burst AE signal considered as a qualitative measure of a discrete signal related to an individual emission event, and (2) a continuous AE signal considered as a qualitative measure of the sustained signal level. The burst AE signal defined as $v_{burst}(t)$ for single frequency f_0 is idealized in order to include the arrival time factor into the formulation as follows

$$V_{burst}(t) = V_0 \sin(2\pi f_0 t)\{(1-e^{-(t-t_{arrival})/t_{rise}}) \in 0...1\} x e^{-(t-t_{arrival})/t_{decay}} H[t-t_{arrival}] \quad (3.1)$$

where the term $\{(1-[\exp(t-t_{arrival})/t_{rise}]) \varepsilon 0 \ldots 1\}$ indicates the rise time function normalized to be in the range of 0-1, t_{rise} is rise time, the term exp $(t-t_{arrival})/t_{decay}$ indicates the decay time with t_{decay}, the term $H[t-t_{arrival}]$ is Heaviside function indicating the waveform arrival to the sensor at $t_{arrival}$. The continuous AE signal $v_{continuous}(t)$ for single frequency f_0 is idealized in as follows;

$$V_{continuous}(t) = \sin(2\pi f_0 t)\sum_{i=1}^{\infty} V_i \{(1-e^{-(t-t_{arrival})/t_{rise}}) \in 0...1\} x e^{-(t-t_{arrival}(i))/t_{decay}(i)} H[t-t_{arrival}(i)] \quad (3.2)$$

As compared to the burst AE signal, the continuous AE signal no definite rise time is apparent, and can be considered as the summation of multiple wave arrivals using Heaviside functions.

3.3.3 Research Methodology

The research methodology in this study is a measure of AE signal in time-domain prior to a conversion to the subsequent frequency-domain using FFT analysis. Fig. 1 shows a steel pipeline with a diameter of 0.5 inches that model the industrial compressed air pipelines. The steel pipeline completely includes a 90°-Degree Elbow (ELL), a T-Shape Elbow (TEE), and Blank-end. The air compressor with an electric regulator provides air pressure with three generally used cases, i.e. 4, 5, and 6 Bars. The AE sensor is attached to only one point at the air in-let on the steel pipeline using grease. The detected AE signals are amplified with a gain of 20 dB prior to an analysis in Labview through National Instrument (NI) DAQ board. Note that the gain of 20 dB since signal swing is less than the power supply of 5 V. Fig. 3.21 shows the experiment equipment, involving the designed pipeline, the air compressor with a regulator, the AE sensor model R80α, and the preamplifier with three variable gains of values 20dB, 40dB, and 60dB. The inspection procedures are performed at four particular points (LP1-LP4), focusing on the joints that vulnerable to air leakage. Fig. 3.23 illustrates the four leak points in the experiments. The results will be obtained through the comparisons of no-leak and leak conditions.

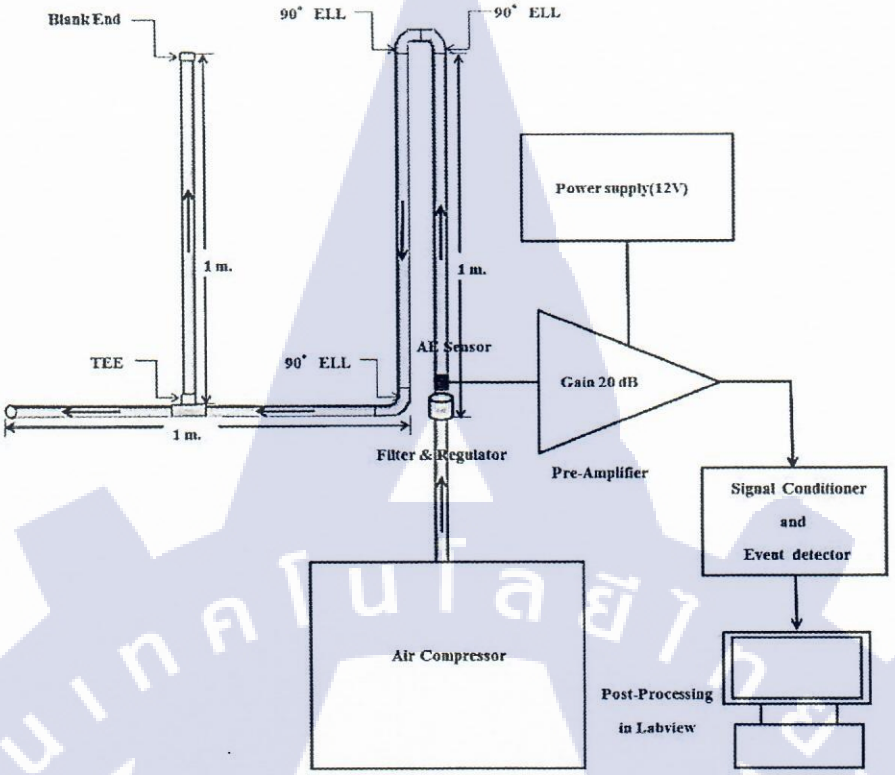

Figure 30: A steel pipeline with a diameter of 0.5 inches that model the industrial compressed air pipelines.

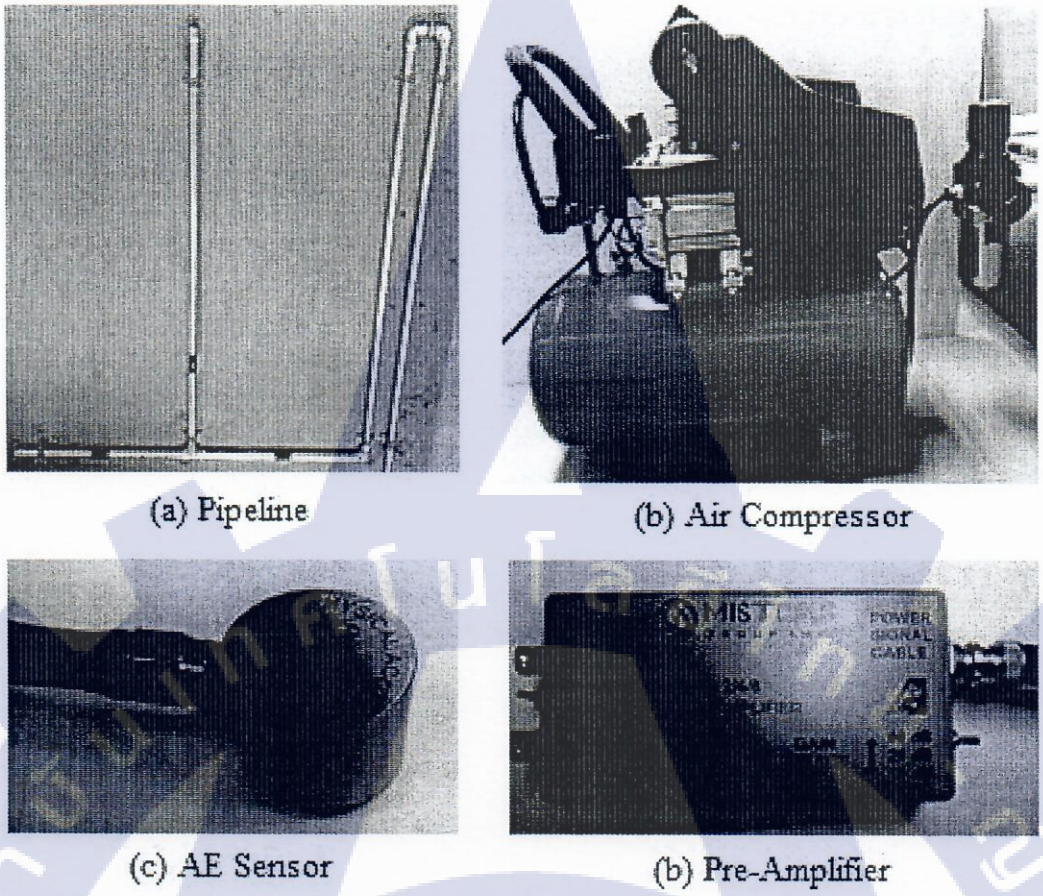

Figure 31: Experiment Equipments, (a) Pipeline, (b) Air compressor, (c) AE sensor, and (d) Pre-Amplifier.

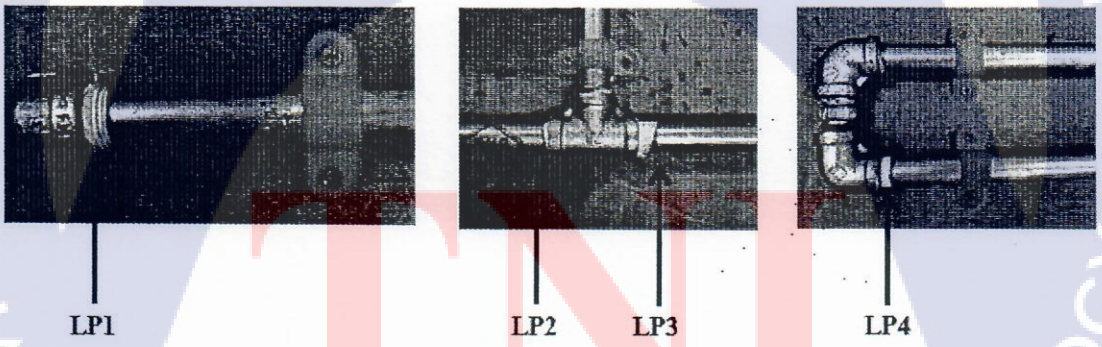

Figure 32 : Four Leak Points (LP1-LP4) focusing on the joints of the air compressed steel pipeline.

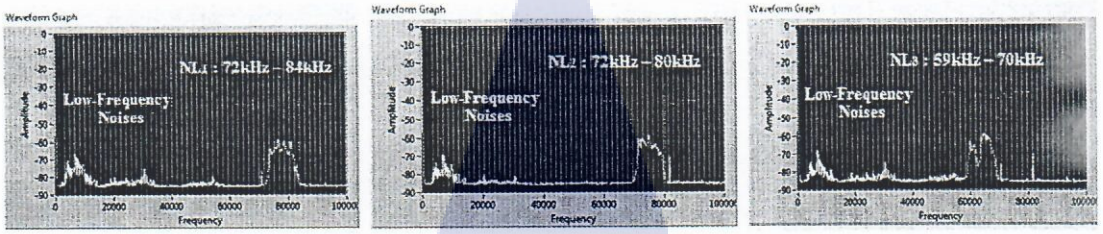

(a) 4 Bars (b) 5 Bars (c) 6 Bars

Figure 33: The frequency responses of measured time-domain AE signals with no-leak conditions at different pressure values of 4, 5, and 6 Bars.

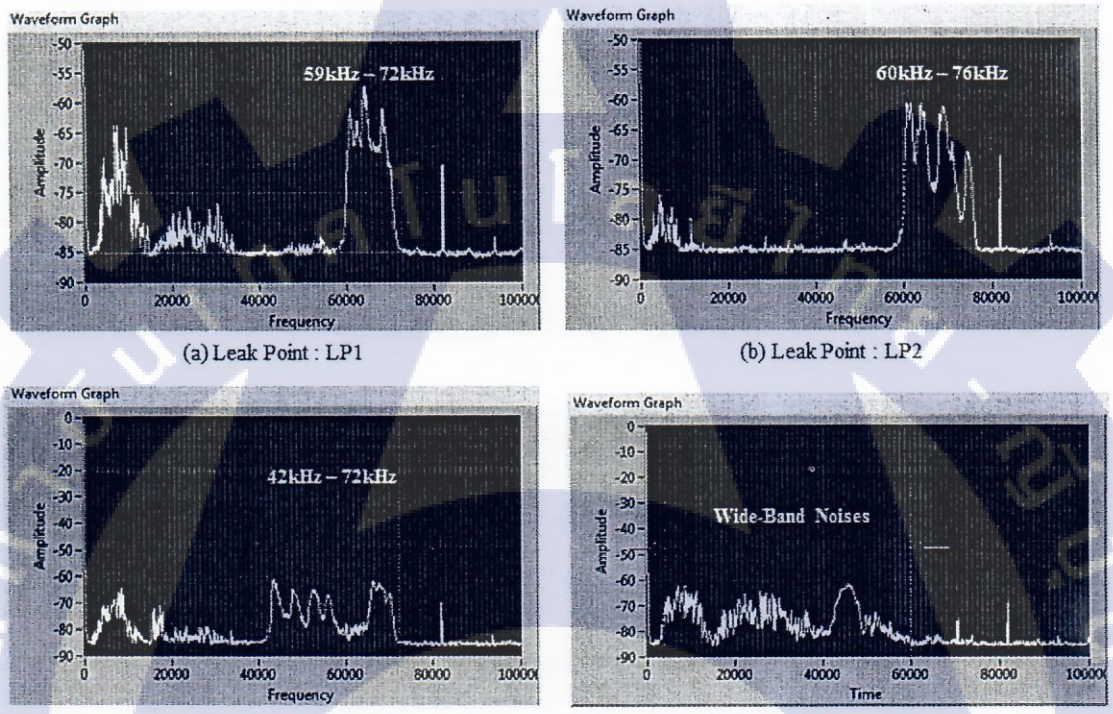

(a) Leak Point : LP1 (b) Leak Point : LP2

(c) Leak Point : LP3 (d) Leak Point : LP4

Figure 34 : The frequency responses of measured time-domain AE signals with four leakages at the pressure value of 4 Bars.

3.3.3 Experimental Results and Analysis

According to the experiment methodology, the results have been achieved through Labview program. For no-leak conditions, Fig. 4 shows the frequency responses of measured time-domain AE signals at different pressure values of 4, 5, and 6 Bars. It can be considered that the frequency bands are oppositely reversible to the increase of pressure values, i.e. NL1: the frequency band of 72kHz – 84kHz is a response band of 4 bars, NL2: the 72kHz – 80kHz is a response band of 5 bars, and NL3 : the 59kHz – 70kHz is a response band of 5 bars. All frequency bands have the magnitude of around -60 dB. In addition, the noises are apparent at low frequency in the range of 0-20kHz while the noise floor is -85dB.

For air-leakage conditions, four cases were observed at three different pressure conditions as previously mentioned. Fig.5 shows the frequency responses of measured time-domain AE signals at the pressure value of 4 Bars. It can be seen that the frequency bands are shifted from the typical value of 72kHz – 80kHz depicted in Fig.3.25 (a). The frequency response of AE signals at leak points LP1, LP2, LP3, and LP4 are 78kHz – 88kHz, 70kHz – 88kHz, 60kHz – 70kHz, and wide-band noise spectrum, respectively.

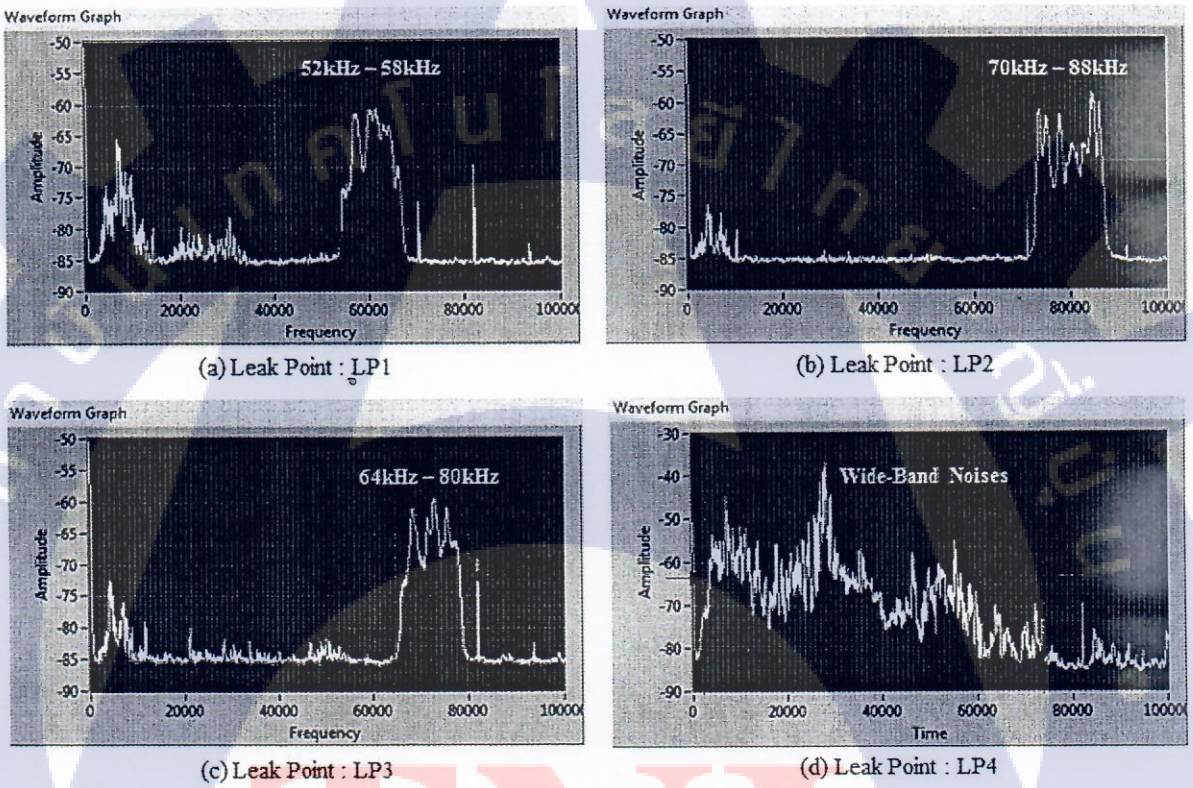

Figure 35: The frequency responses of measured time-domain AE signals with four leakages at the pressure value of 5 Bars.

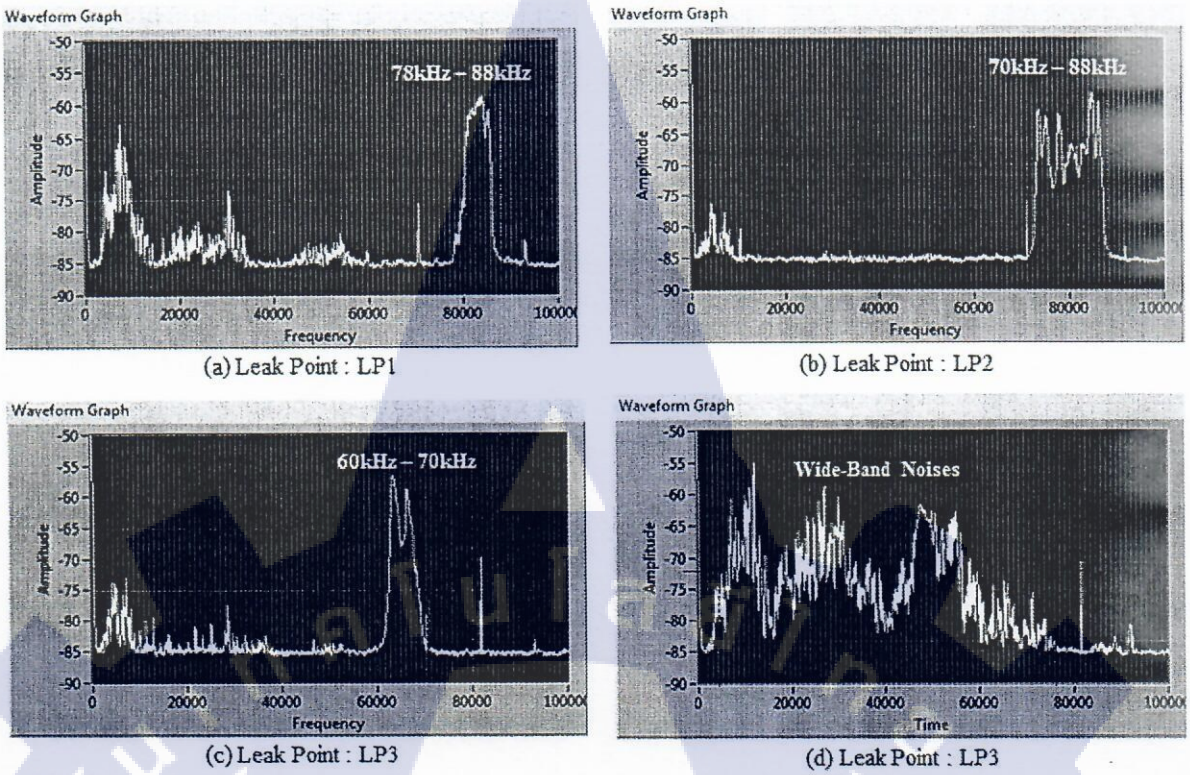

Figure 36 : The frequency responses of measured time-domain AE signals with four leakages at the pressure value of 5 Bars.

signals at the pressure value of 5 Bars. Apparently, the signal also shifted from the typical value of 72kHz – 80kHz depicted in Fig.5 (6). The frequency response of AE signals at leak points LP1, LP2, LP3, and LP4 are 52kHz – 58kHz, 70kHz – 88kHz, 64kHz – 80kHz, and wide-band noise spectrum, respectively. Fig.3.27 lastly shows the frequency responses of measured time-domain AE signals at the maximum pressure values of 6 Bars. The results are in a similar manner of the cases of 4 and 5 Bars. The frequency response of AE signals at leak points LP1, LP2, LP3, and LP4 are 78kHz – 88kHz, 70kHz – 88kHz, 60kHz – 70kHz, and wide-band noise spectrum, respectively. Based on the experimental results from Figs.5-7, it can be considered that the frequency bands are shifted from the typical value, demonstrating that the proposed method can be used to detect the air leakage in the air pressured pipeline.

3.3.4 Conclusions

A compressed air piping system has long been employed as commercial industrial facilities, and considered as a utility essential to production. The non-destructive inspection using acoustic emission sensors have been suggested as effective inspection techniques in fluid transfer

piping system. However, most previously proposed techniques employed complicated measurement algorithms or required many AE sensors, resulting costly implementation. Moreover, the results require specific software with a skilled expertise to read the signal features. This work has therefore presented a cost-effective AE sensing system for industrial application where a single AE sensor is realized for signal characterizations through Fast-Fourier Transform (FFT) algorithm. Experiments were realized through a steel pipeline with a diameter of 0.5 inches to model the industrial compressed air pipelines, completely including a 90o-Degree Elbow (ELL), a T-Shape Elbow (TEE), and blank-end. The AE signal was amplified with 20 dB prior to an analysis in Labview through National Instrument (NI) DAQ board. Air pressure with four cases, i.e. 4 to 6 Bars, were investigated. The results revealed that the frequency response of AE signals between no-leak and leak conditions could be inspected accurately through the shift in frequency bands. This work has presented an alternative potential for a cost-effective AE characterization methods in industrial applications.

4. Intelligent Feedback Control System

4.1 An Intelligent Wireless Mulit-Sensor Temperature Control System using a Self-Tuning PID Contoller with Neural Networks

Air conditioning system typically controls the temperature in a closed area at a constant value and the temperature deviation should not exceed 2 oC as for generally acceptable temperature criteria in industrial plants. The typically and commercially available on-off temperature control system operates by sensing temperature and sending the control signals to stop the the compressor when the temperature is higher than the preset value. Consequently, the temperature is not stable due to start-stop operation, resulting in the short life-time of compressor motor. In addition, such a system also consumes much energy for starting the motor repeatedly.

As a potential alternative to the on-off control system for air conditioner, the use of a Proportional-Integral-Derivative (PID) controller still remains as a common control algorithm in industry. The PID controller offers versatility, high reliability and ease of operation [35]. Nonetheless, the performance of PID controller degrades during operational time owing to process non-linearity or process time varying parameters, and consequently retuning process is ultimately required [36]. Moreover, Retuning such a PID

controller is mostly performed through a trial-and-error procedure which is a time consuming process and only skillful operators could effectively adjust to suitable operational conditions. As a results, there has been extensive research attempts to find the effective tuning procedures for PID controllers.

The trend of system control techniques has recently focused on artificial intelligent and fuzzy logic techniques. Nonetheless, the fuzzy logic control may not stable in some circumstances, and difficult for hardware implementations [37-38]. Therefore, an artificial Neural Network (ANN) has become a promising solution for nonlinear system controls with capability of learning the problems, predicting the next solution, and providing low response time with high precision. In terms of system identification and control applications, the feed forward multilayer neural networks are the most widespread architecture using a back propagation training algorithm.

In the field of temperature control systems, there have also been attempts to apply ANN for controlling temperatures. N. Rai and B. Rai [39] presented the PID gain controls using approximation through ANN. S. Kim and S. Jung [40] proposed the use of ANN that imitates the operation of PID controller. A. Al-Ghasem and N.Ussaleh [41] employed the ANN model to predict and control the temperature and energy consumption in buildings. In particular, X. Liu [42] proposes the frequency control of air conditioner through the use of ANN. Specific PID controllers for mortar control also found in [43-44]. Despite the fact that ANN has been applied to motor controls with high precision operations, it has been found that all previous works employed only a single temperature sensor which may not be suitable for a large room.

This work therefore presents an intelligent and automatic temperature control system for a stable room temperature. Multi-sensor temperature sensing system with wireless data transmission is designed in order to achieve accurate temperature measurement over a wide area. The control system is a PID controller with self-tuning feature using an artificial neural network. The wireless control system is designed through cost-effective

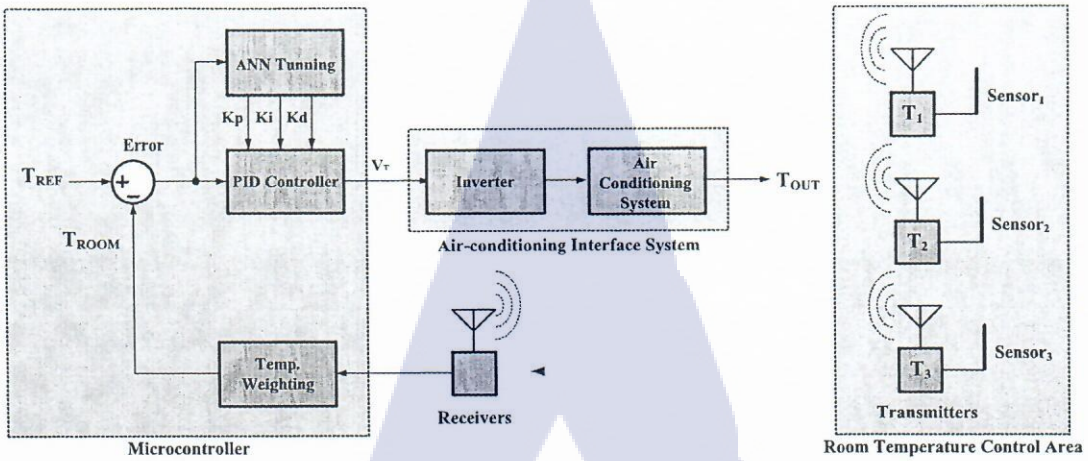

Figure 37 : The overall wireless multi-sensor industrial temperature control system.

temperature sensor, transceiver and Arduino microcontroller. The controller provides a control signal to VSD to control speed of motor compressor. The experimental results using a modified air conditioner of 24,000 BTU reveal a fast and stable setting of any specifically set temperatures.

4.1.1 Overall Architecture

The overall architecture of the proposed wireless multi-sensor industrial temperature control system is depicted in Fig.4.1. It can be seen in Fig.4.1 that the system consists of three major sections. First, the PID controller and the ANN tuning system with weighting algorithm are implemented by a microcontroller. The PID controller accepts the errors between the primary set temperature Tref and the actual temperature Troom. The error is also used for tuning the three gains Kp, Ki, and Kd of the PID controller through the ANN tuning system. It can also be seen that the Temperature weighting algorithm is also included for averaging the actual temperature sensors to a single value.

Second, the air conditioning system consists of the inverter which accepts the voltage value in the range of oV to 5V that sets the maximum and minimum speed of the motor and hence the output temperature Tout. Last, the three wireless temperature sensors are implemented for the three locations in the room, including the front of the air conditioner and the two locations in the back of the room. The multi-sensor systems have been implemented in order to average the temperature at different locations in the room. The wireless transmission system is equipped for transmitting data without any difficulties in wiring the temperature sensors. It can be

concluded that the proposed system is newly designs not only for the multi-sensor system but also the intelligent controller using artificial neural networks tuning for the PID controller.

4.1.2 Wireless Temperature Sensor Designs

The wireless systems have been designed using the microcontroller-based system. For the temperature sensor, the model DHT11, which is a temperature and humidity sensor, has been employed. This DHT11 sensor is cost-effective and provides a calibrated digital signal output with 8-bit microcontroller. The measuring temperature range is between 0OC to 50 OC with the power supply of 3.5V to 5V. The transmitter and receiver are implemented by the model nRF24L01. This transceiver model is a cost-effective data transmitter and receiver in a single chip operating at 2.4GHz ISM band and the data rate is relatively high up to 2Mbps. Fig.4.2 shows the design and implementation of the wireless temperature sensor and transceiver system. In Fig.4.2 (a), the temperature sensors sense the room temperature and send the data to the microcontroller as an interface unit to the transceiver prior

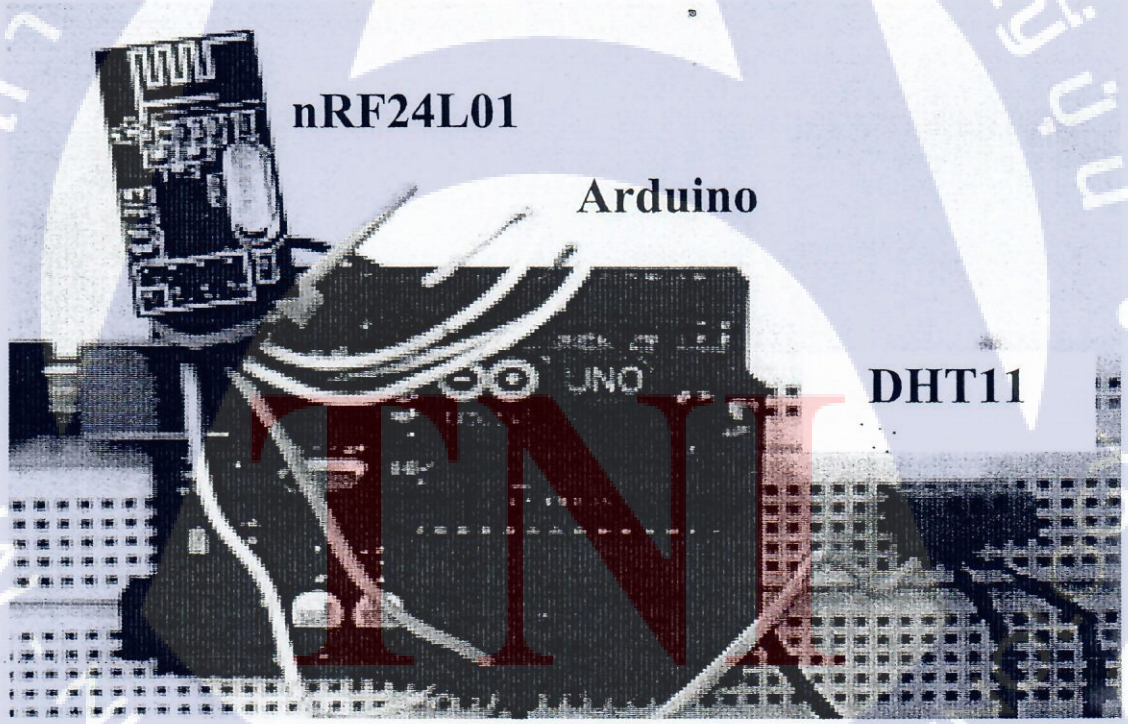

(a) The temperature sensor and the transmitter.

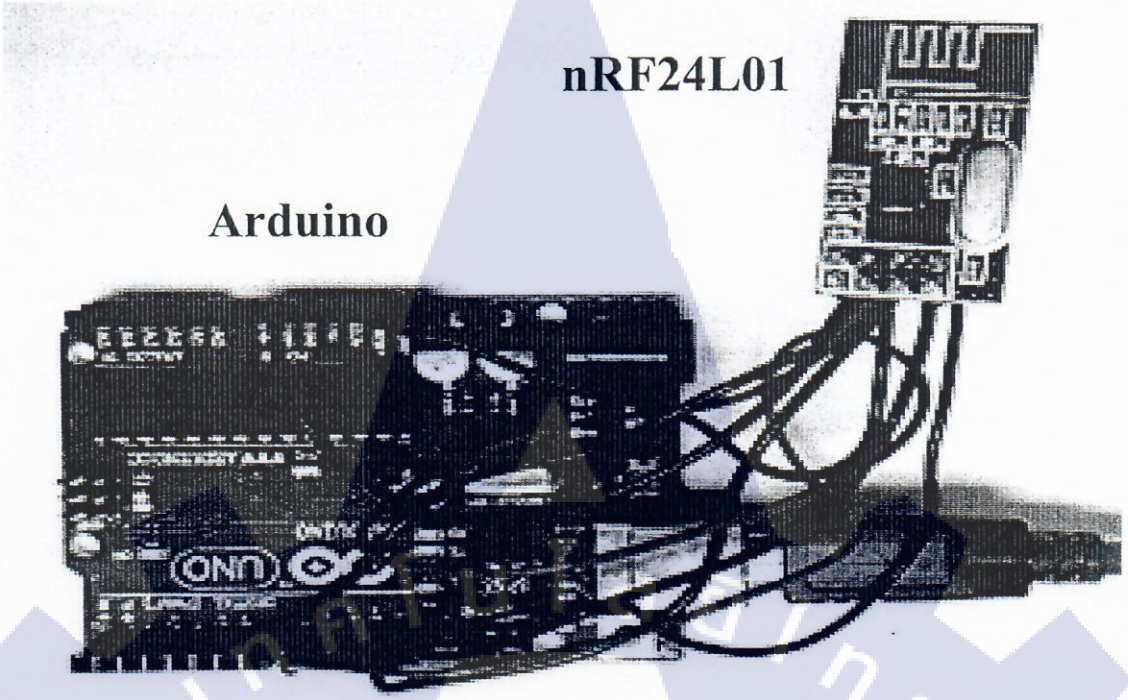

(b) The receiver and the controller.

Figure 38: The design and implementation of the wireless temperature sensor and transceiver system.

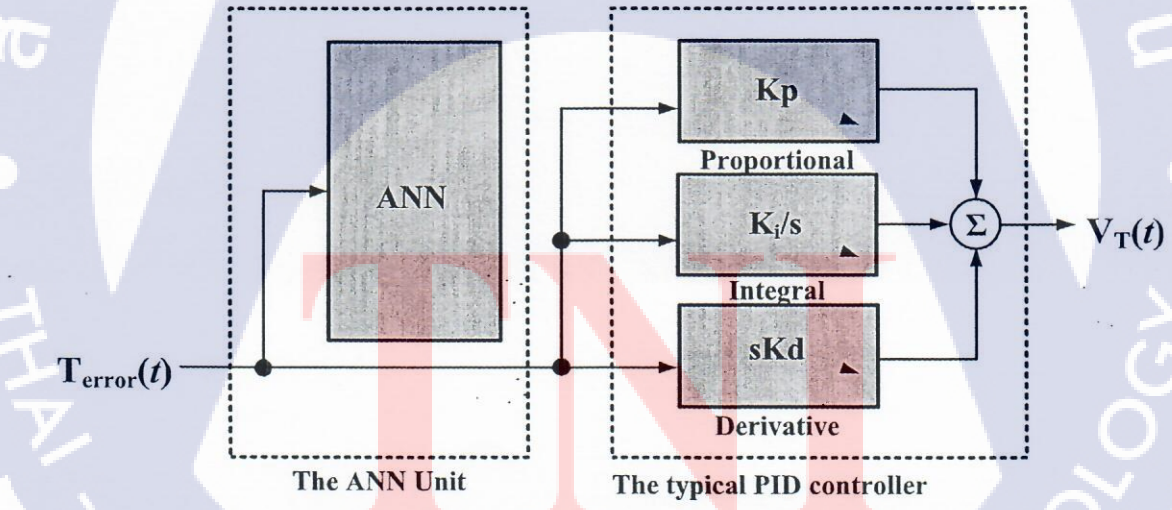

Figure 39 : The PID controller with self-tunning of PID gains using nueral network.

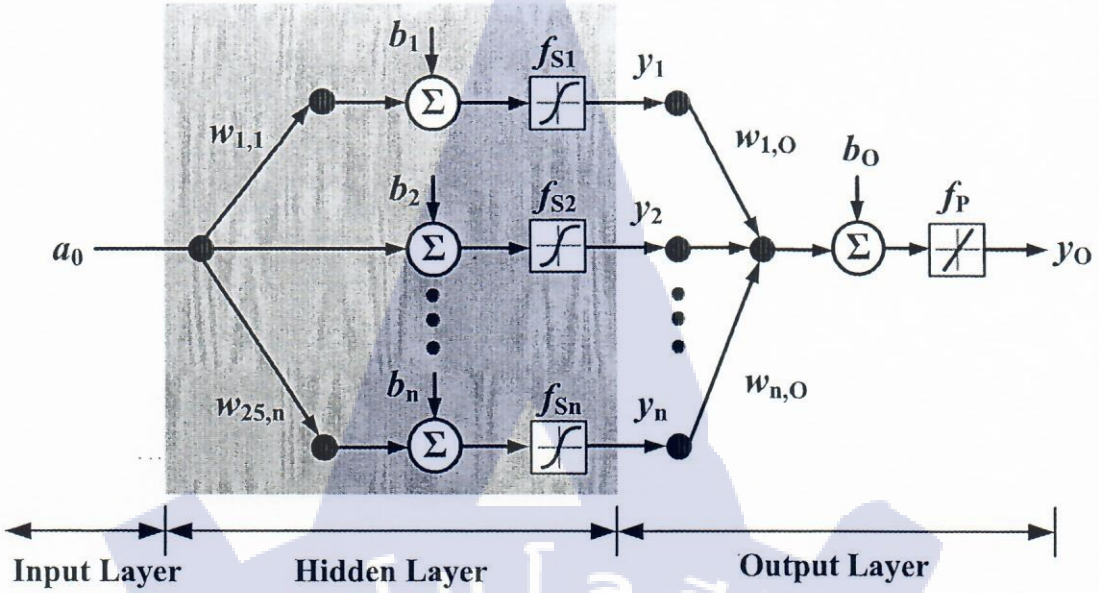

Figure 40 : The designed and optimized back propagation neural network.

to the wireless data transmission to the base station. In Fig.4.2 (b), the receiver receives the data from all sensors and weights for the average temperature. In addition, this controller also implements the PID controller and the ANN tuning units. The primary set values for the room temperature is 25OC.

4.1.3 PID Controller Designs

Figure 3 shows the PID controller with self-tuning of PID gains using neural network. The typical form of the PID controller is given by

$$V_T(t) = k_p T_{err}(t) + k_p \int_0^t T_{err}(t) d\tau + k_d \frac{dT_{err}(t)}{d\tau} \qquad (4.1)$$

The output $V_T(t)$ is the control voltage output in the range of 0V-5V which is used to drive the motor speed that ultimately sets the air temperature through the compressor. The error temperature Terr(t) = Tref(t) – Troom(t) is the error temperature obtained from the difference between the preset

temperature and the weighted temperature of three sensors. The values of this Terr(t) changes corresponding to the change in room temperature.

With reference to Fig.4.3 and Eq. (1), there are three sub-blocks. The proportional controls the loop gain in order to make the system less sensitive to load disturbances, the integral of error is used to eliminate the steady-state errors, and the derivative of errors is used to improve closed loop stability. In addition, the PID gains Kp, Ki, Kd are set in order to meet prescribed performance criteria in terms of rise and settling times, overshoot and steady-state error. In this work the values of these gains are primarily set to Kp =624.57, Ki=1355.56, and Kd=50.13. These values are obtained from the optimized procedure using MATLAB Simulink. The gains are automatically tuned by ANN through a summation of values from the ANN.

4.1.4 Artificial Network Designs

Fig.4.4 shows the structure of designed and optimized back propagation neural network as a controller for the boost converter. This ANN is initially trained for a required certain output value. The realized ANN topology is kind of back propagation multi-layer perceptron, which is a class of supervised learning neural networks, and is suitable for applications in, for instance, data classification and approximation. It is seen in Fig.4.4 that the ANN comprises three layers, i.e. input, hidden, and output layers. The input layer is an error temperature Terr(t). The hidden layer then processes the input digital signals through weighting, biasing, and mapping operations. This work realizes a Hyperbolic Tangent Sigmoid (tansig) activation function in the hidden layer described as

$$y_n = \text{tansig}\left(\sum_{i=1}^{n} a_b w_{b,n} + b_n\right) \qquad (4.2)$$

where ao represents the input value. wb,n is a weight for each input bit at nth-node and b=25. bn is a bias for nth-node. In fact, the values of n can be obtained from the trial-and-error process till optimization is found. Last, the output layer processes the outputs from the hidden layer using pure line (pureln) activation function as follows

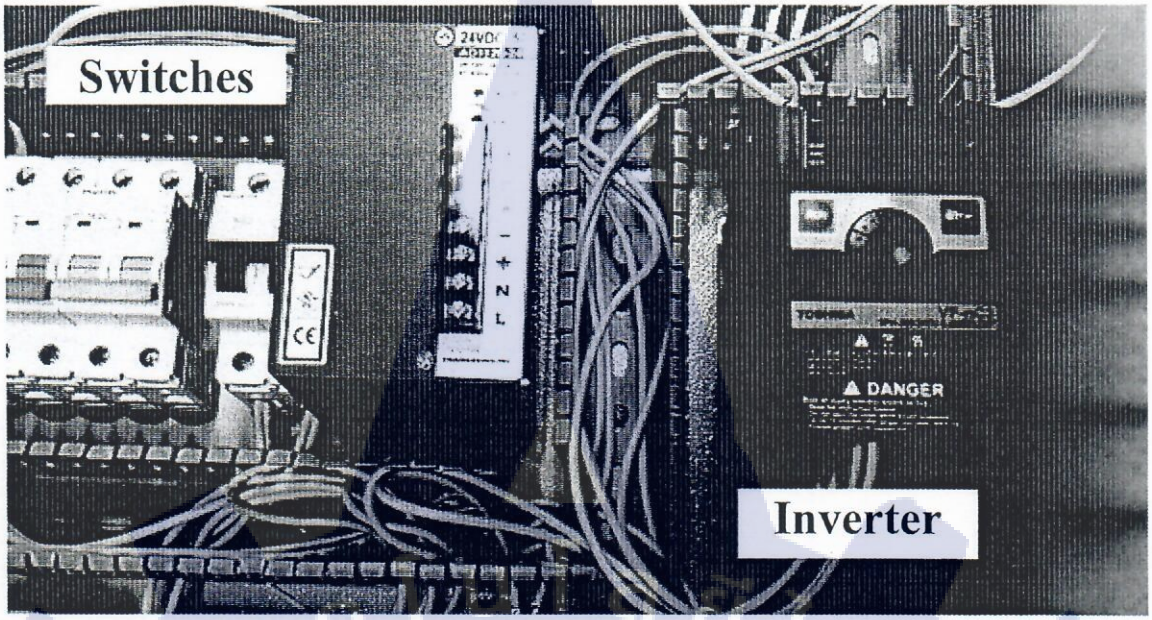

Figure 41 : The photograph of the inverter model VF-nC3 that controls speed of motor compressor of the modified 24,000-BTU air conditioner.

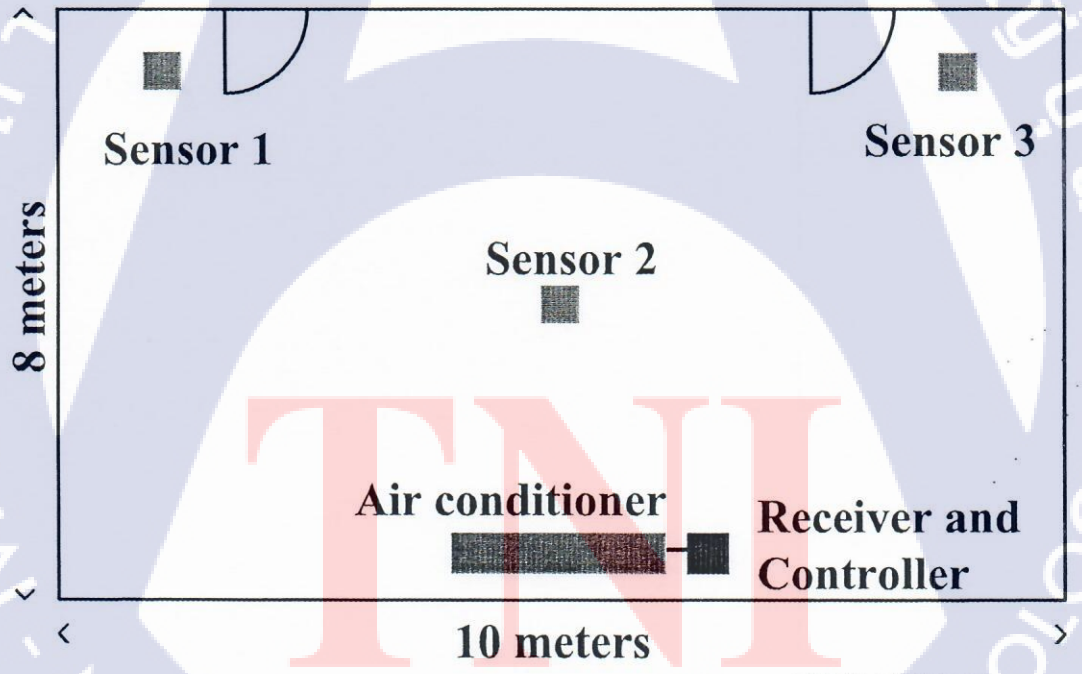

Figure 42 : The locations of the temperature sensors in a closed area.

$$y_O = \text{pureln}(\sum_{i=1}^{n} y_n w_{n,O} + b_O) \quad (4.3)$$

where yn represents the output from the hidden layer at nth-node. wn,O is a weight for each hidden layer output from nth-node. b_O is a bias of the output layer. It can be considered that the performance of the ANN depends upon the number nodes in the hidden layer. This work also optimizes such number nodes in order to find the appropriate node numbers in terms of operating speed and complexity. Fig. 4.5 shows the structure of the trained neural network. It can be seen from Fig. 4.5 that the optimized structure has 25 hidden layers and 3 output layers for the PID gains Kp, Ki, Kd. As shown in Fig.6, The training method is Levenberg-Marquardt (LM) and the performance was set to 10×10-3 and it achieves at the iterations of 31 epochs.

4.1.5 Experimental Results

The experiments have been performed through the use of the modified air conditioner of a 24,000 BTU controlled by the VF-nC3 that controls speed of motor compressor as shown in Fig.7. The sensors were placed at three locations in a closed area of 8m×10m. The room temperature was early set at a very low temperature of 12^{O}C in order to investigate the tremendous changes in temperature and the effectiveness of the proposed system implementation. The temperatures were monitored through the average or weighted temperature obtained from the microcontroller. Fig. 4.7 shows the measured results of the temperature from the microcontroller showing a stable temperature of 25^{O}C. The system could quickly reset to the set value within approximately 15 minutes. The system keeps operate at stable temperature of 25^{O}C throughout the operating day.

4.1.6 Conclusion

This work has presented the practical implementation of the intelligent temperature control system. The system employs the multi-sensor temperature sensing system with wireless data transmission. The control system is a PID controller with self-tuning feature through the artificial neural network. The experimental results show a fast and stable setting of any specifically set temperatures. The proposed temperature control system can be applied to a stable temperature for industrial plant, energy saving, and

long life time of air conditioner. The future works include the enhancement of ANN-PID controller and the tests under different environment conditions.

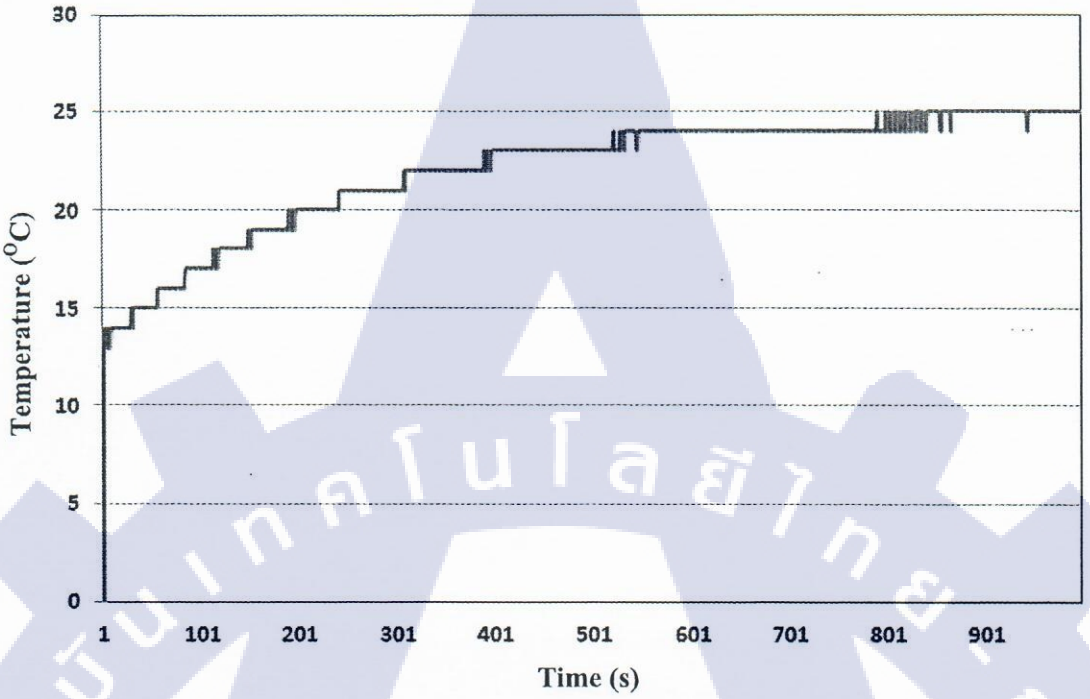

Figure 43: The measured results of the temperature from the microcontroller showing a stable temperature of 25°C.

5. Intelligent Nonlinear Dynamic Systems for Secure Communications and Data Storage

5.1 The Development of an Android Application for Image Cryptography Using the Chaotic Map with Absolute Value Nonlinearity

5.1.1 Introduction

Chaotic map is an iterated function in a discrete time-domain which can generate chaotic behaviors. Chaotic maps also possess significant properties, including the sensitivity to initial conditions and system parameters which leads dynamic behaviors. Recently, various chaotic maps have been employed in many fields of research. In the field of computer security, there have been a number of chaotic maps proposed for encryption and decryption. For instance, four chaotic maps with absolute value nonlinearity which has a random bit generator that passed randomness tests using National Institute of Standards and Technology (NIST) statistical test

suite have been proposed [45, 46]. The design of the random bit generator using the skew tent map which also passed all NIST tests has been proposed in [47], and the pseudo-random binary sequence generation using two-dimensional Hénon map has also been proposed in [48]. In the field of image cryptography, an image encryption technique using two-dimensional Baker map on a gray scale image which tested by using 28 characters or 64 bits cipher keys which are 1 bit different to each other, has been proposed in [49]. The image encryption which employs multiple chaotic maps including logistic map, tent map, quadratic map, and Bernoulli map as layers of chaotic maps have been suggested by [50]. Android is one of the most popular mobile platforms which give developers a platform for applications development and an open marketplace for distributing the developed applications [51]. Chaotic maps also been implemented in the Android application development, such as the recent research which proposed an Android application development which used the Hénon map in the chaotic steganography for the secure image transmission and reception [52].

One recent research which generalizes one case of the chaotic map with absolute value nonlinearity as an Android application in terms of time-domain chaotic waveforms, frequency-domain waveforms, bifurcation diagram, and the Lyapunov Exponent (LE) spectrum was already presented in [45]. This work aims to implement one case of the chaotic maps with absolute value nonlinearity in image cryptography on Android. This work is the demonstration and implementation of the chaotic maps with absolute value nonlinearity in the Android application development in the field of image cryptography. The results from experiments of the proposed application on an Android emulator are also included.

Chaotic maps with absolute value nonlinearity were proposed in the recent research in four cases [46]. These chaotic maps with absolute value nonlinearity have been tested for the robustness and simplicity by having sequences generated from each case passed all tests in NIST statistical test suite in all cases. However, the case which is implemented in this work is the first case which described as

$$x_{(n+1)} = |1 - ax_n| \tag{5.1}$$

where a is a control parameter and in the range of [0, 2].

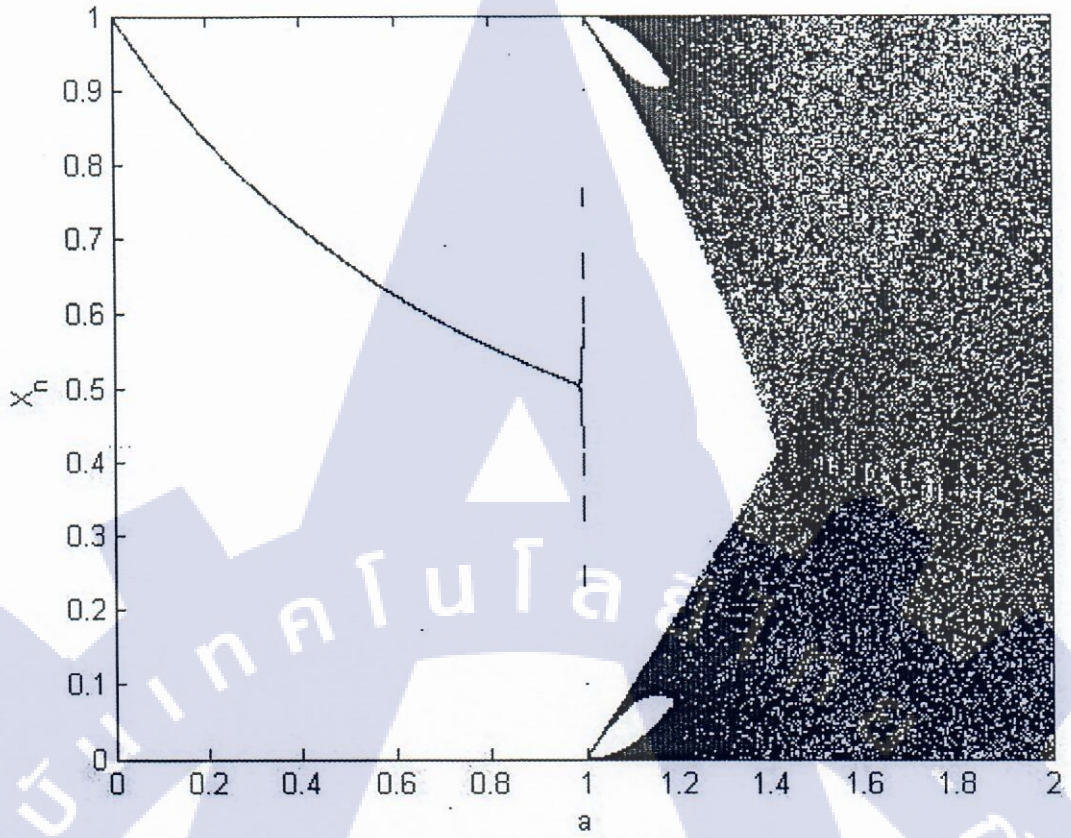

Figure 44: Bifurcation of (5.1) where the control parameter a is in [0, 2].

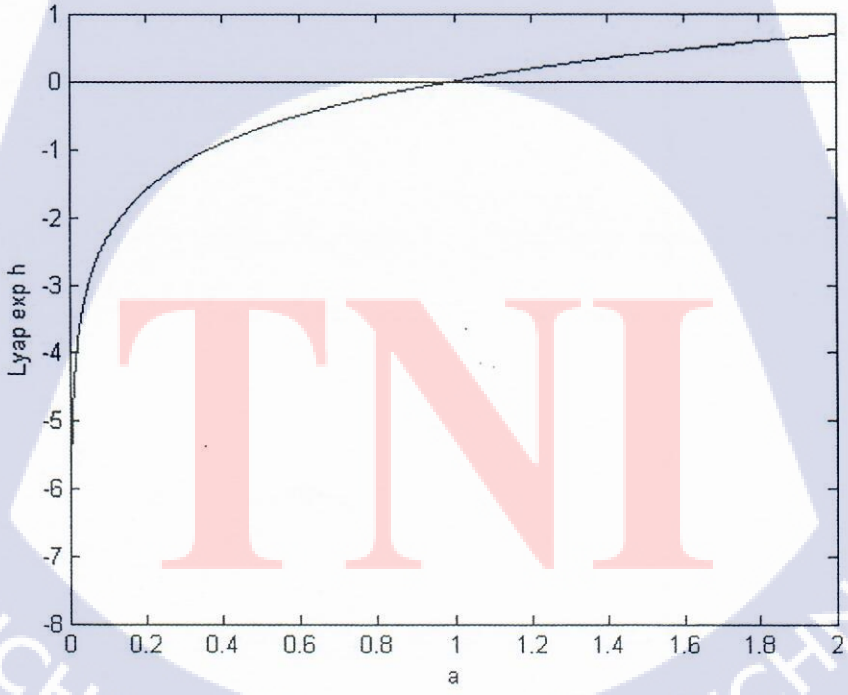

Figure 45 : LE spectrum of (5.1) where the control parameter a is in [0, 2].

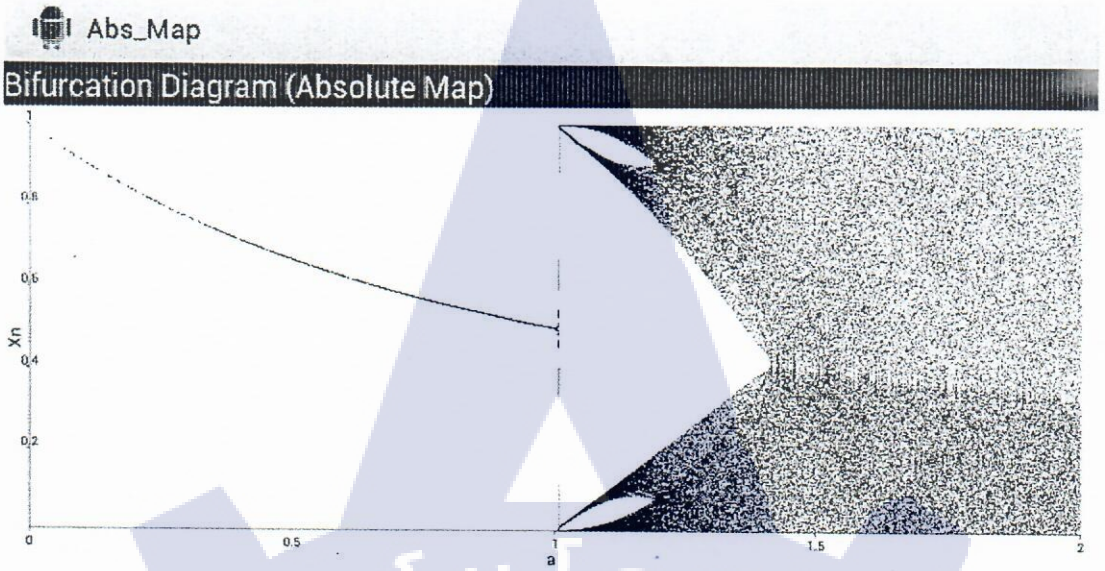

Figure 46: Bifurcation diagram of (5.1) where the control parameter a is in [0, 2] on an Android application.

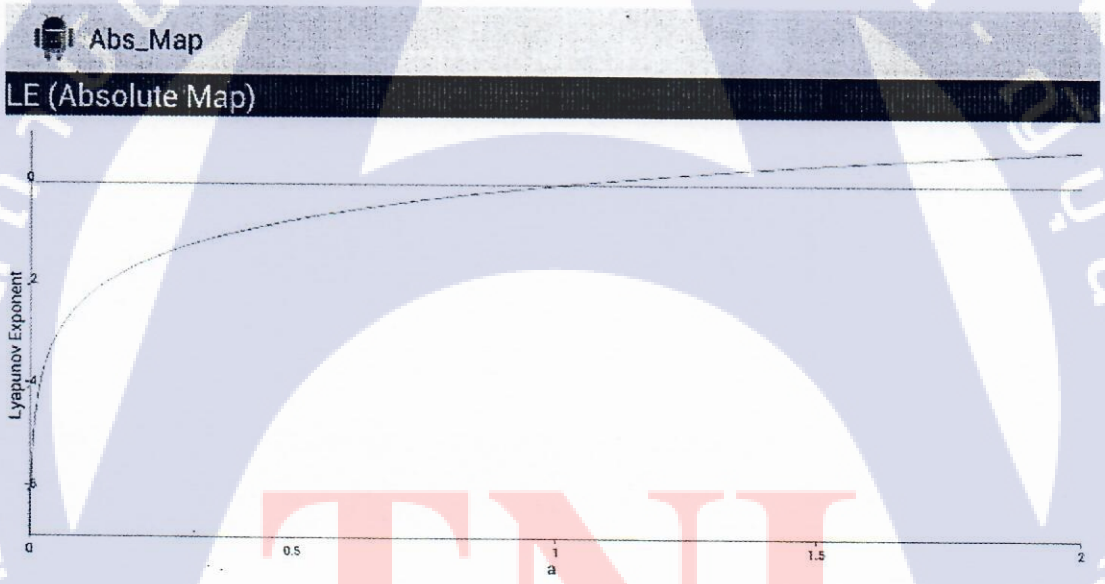

Figure 47 : LE spectrum of (5.1) where the control parameter a is in [0, 2] on an Android application.

$$\lambda = \lim_{n\to\infty}\left(\frac{1}{N}\right)\sum_{n=1}^{N}\ln f'(x_n) \qquad (5.2)$$

where N is the number of iterations, λ is the LE, and f '(x) is the first derivative of the chaotic map. Fig. 5.2 shows the LE spectrum of (1) from MATLAB. The system tends to be more chaotic as the value of LE rises and

the system become chaotic when the value of LE is more than 0. From the LE spectrum in Fig. 5.2, the value of LE is more than 0 when a in the range of [45, 46] which is the same region that chaotic behaviors are occurred in the bifurcation diagram. The bifurcation diagram and the LE spectrum of (1) indicate that the chaotic map with absolute value nonlinearity tends to be more chaotic as the value of the control parameter a is closer to 2. The recent research which generalized the first case of the chaotic maps with absolute value nonlinearity on an Android application also had similar results to the results from MATLAB. Fig. 5.3 and Fig. 5.4 shows the bifurcation diagram and the LE spectrum of (1) from the Android application proposed in the research respectively.

The simplicity, the robustness, and the compatibility with Android are three main conditions which results in the first case of the chaotic maps with absolute value nonlinearity been elected to be implemented in this work. where N is the number of iterations, λ is the LE, and f '(x) is the first derivative of the chaotic map. Fig. 5.2 show the LE spectrum of (1) from MATLAB. The system tends to be more chaotic as the value of LE rises and the system become chaotic when the value of LE is more than 0. From the LE spectrum in Fig. 5.2, the value of LE is more than 0 when a in the range of [45, 46] which is the same region that chaotic behaviors are occurred in the bifurcation diagram. The bifurcation diagram and the LE spectrum of (1) indicate that the chaotic map with absolute value nonlinearity tends to be more chaotic as the value of the control parameter a is closer to 2. The recent research which generalized the first case of the chaotic maps with absolute value nonlinearity on an Android application also had similar results to the results from MATLAB. Fig. 5.3 and Fig. 5.4 shows the bifurcation diagram and the LE spectrum of (1) from the Android application proposed in the research respectively.

The simplicity, the robustness, and the compatibility with Android are three main conditions which results in the first case of the chaotic maps with absolute value nonlinearity been elected to be implemented in this work.

Table 5.1

The Configurations of an Android Emulator.

Configurations	Selected options/values
Device	5.1" WVGA(480 x 800 mdpi)
Target	Android 4.4.2 – API level 19
CPU/ABI	ARM (armeabi-v7a)
Skin	Skin with dynamic hardware controls
Back camera	None
RAM	512 MB
VM heap	64
Internal storage	512 MB
SD card	512 MB

5.1.2 Development and Experiment Environments

Android applications development can be completed on various development tools. However, the tool which was implemented in this work is the ADT. Android Development Tools (ADT) is a plug-in for the Eclipse Integrated development environment (IDE) which used to be an official IDE of the Android application development prior to December, 2014. The ADT is designed to give Android application developers an integrated environment which can build Android applications. The ADT extends the capabilities of Eclipse to let developers set up new Android projects, create an application UI, add packages based on the Android Framework API, and debug applications using the Android SDK tools included in the ADT [55].

ADT also includes an Android Virtual Device Manager that is capable of creating and managing an Android Virtual Device (AVD) which is an emulator configuration that allows developers to model a device by defining hardware and software options to be emulated by the Android emulator. The Android emulator replicates most of the hardware and software features of a typical Android device except actual phone calls on a computer. The Android emulator also allows Android application developers to develop, prototype, and test Android applications without using a physical Android

device [56]. The configuration of the Android virtual device which is emulated and implemented as the device for the Android application experiment in this work is illustrated in Table 5.1.

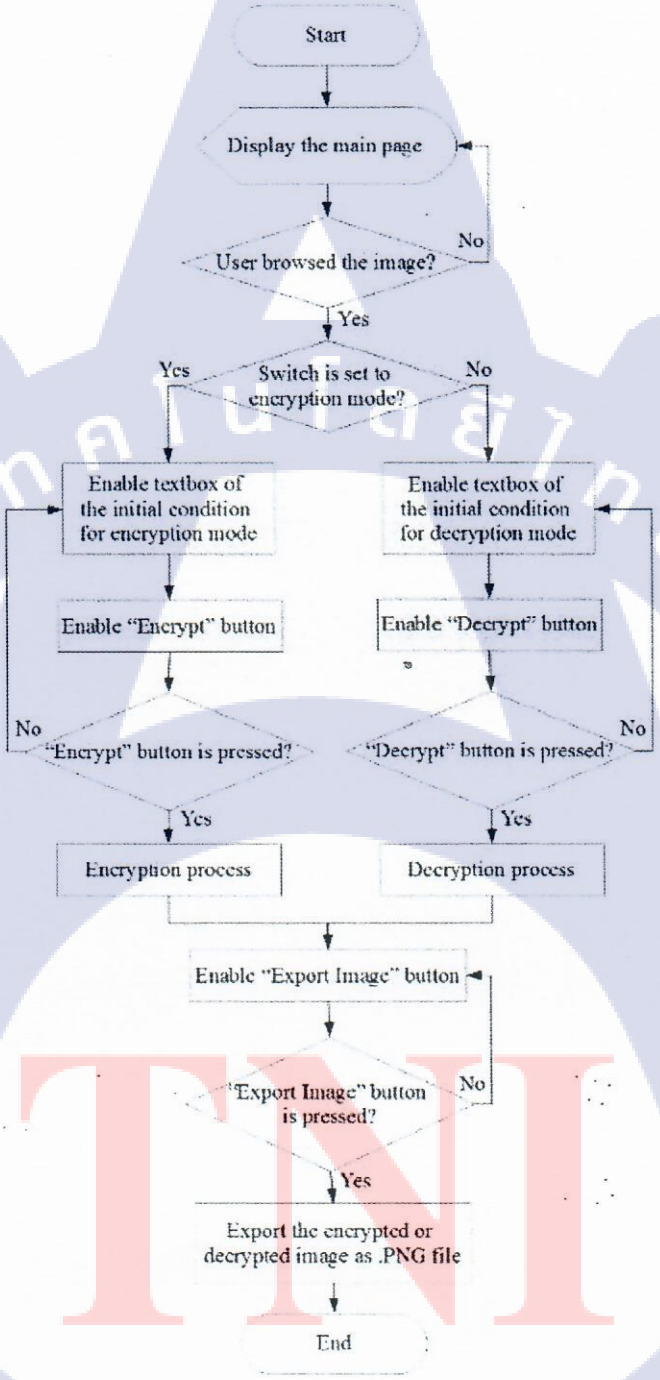

Figure 48 : Flow chart of the proposed Android application.

5.1.3 The Proposed Android Application

The proposed Android application which the flow chart of the application displayed in Fig. 5.5 include 2 main processes which are the encryption and the decryption. Both encryption and decryption process possess similar features which are the implemented chaotic map which is the first case of the chaotic map with absolute value nonlinearity (1), and the image acquisition process which acquires an image from users and converts the acquired image into bitmap.

The algorithm of the proposed Android application starts with the image acquisition process which acquires an image chosen from images in the Android device. The acquired image then converted into a RGB bitmap image with the same dimension of the acquired image and displayed on the screen of the device. The application then prompt the user to input their desired password which are 16 alphanumeric characters defined as A=A0A1A2...A15.

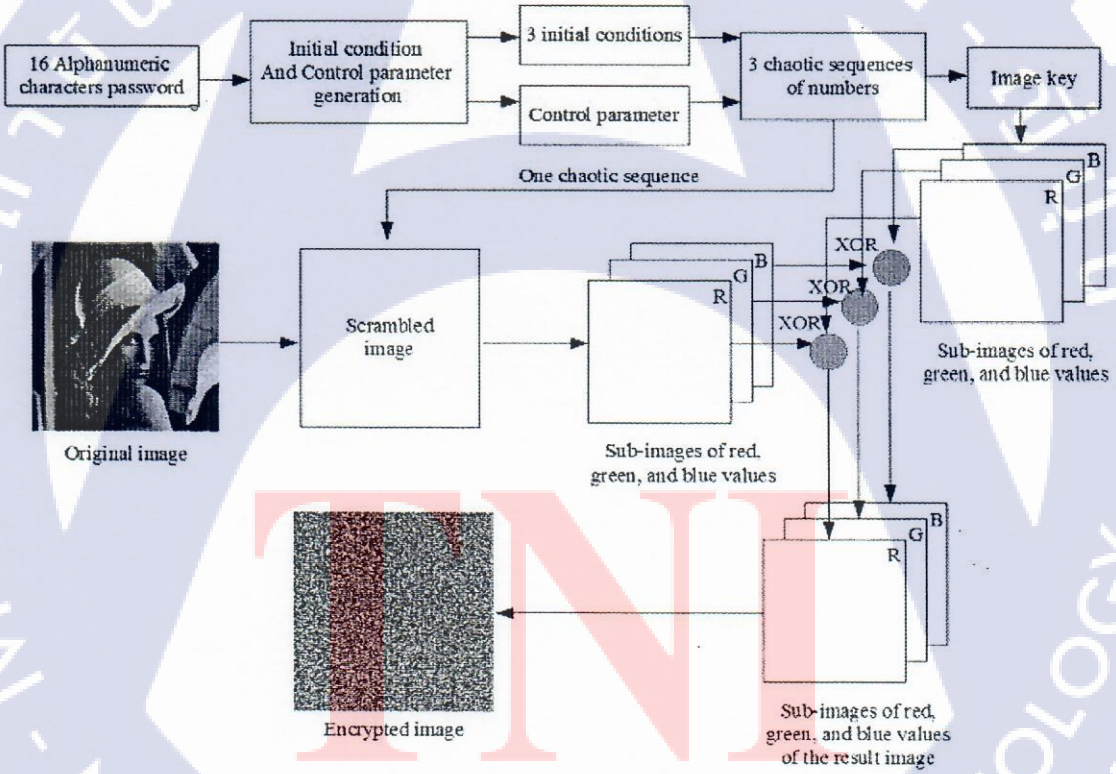

Figure 49 : Block diagram of the encryption process.

The encryption process as displayed in Fig.6 starts after the user pressed the "Encrypt" button by employing the password A into the initial conditions and the control parameter generation for implementing in (1). The process of initial conditions and the control parameter generation starts by separate the alphanumeric password A into 3 sets of ASCII codes X, Y, Z as described in Table 5.2. The 3 sets of ASCII codes are then converted into 42-bit binary representations defined as B_{X0} to B_{X41}, B_{Y0} to B_{Y41}, and B_{Z0} to B_{Z41}. The binary representations are then converted into the real numbers as

$$c1 = (B_{X0} * 2^{41} + B_{X1} * 2^{40} + \ldots + B_{X41} * 2^{0})/2^{42} \quad (5.3)$$

$$c2 = (B_{Y0} * 2^{41} + B_{Y1} * 2^{40} + \ldots + B_{Y41} * 2^{0})/2^{42} \quad (5.4)$$

$$c3 = (B_{Z0} * 2^{41} + B_{Z1} * 2^{40} + \ldots + B_{Z41} * 2^{0})/2^{42} \quad (5.5)$$

After the real numbers are calculated, The real numbers calculated from the alphanumeric password by (1), (2), and (3) are then implemented in the 3 initial conditions ; I_r, I_g, and I_b and the control parameter a generation by

$$I_r = (c1 * c2) \bmod 1 \quad (5.6)$$

$$I_g = (c1 * c3) \bmod 1 \quad (5.7)$$

$$I_b = (c2 * c3) \bmod 1 \quad (5.8)$$

$$a = ((c1 * c2 * c3) \bmod 1 * 0.1) + 1.9 \quad (5.9)$$

The 3 initial conditions I_r, I_g, and I_b and the control parameter a are then employed in (1) to create 3 chaotic sequences of numbers Sr, Sg, and Sb respectively with the same dimension as the number of pixels in the acquired image. The chaotic sequences are then implemented in the image key generation by setting each pixel of the new blank bitmap image with numbers multiply by 255 in Sr for the red value, numbers Sg for the green value, numbers Sb for the blue value, and 255 as the alpha value of the pixel. The sequence of numbers Sr is then employed into the image pixels scrambling before continuing to the XOR operation.

Table 5.2

Summary of the 16 Alphanumeric Characters Password for the Initial Conditions and the Control Parameter Generation.

Set	Characters
X	$A_0A_4A_2A_8A_6A_{10}$
Y	$A_{15}A_{11}A_{13}A_7A_9A_5$
Z	$A_3A_1A_{14}A_{12}A_9A_8$

The generated image key are then employed in the XOR operation with the displayed bitmap RGB image which is converted from the acquired image from the user by XOR each pixel value in each color plane at the same pixel position P(x, y) of the displayed bitmap RGB image with each pixel value in the same color plane, i.e. pixel value in red plane at P(0, 0) of the displayed bitmap RGB XOR with the pixel value in red plane at P(0, 0) of the key image. The pixels values in each color which passed the XOR operation are then employ in the result image creation by setting each pixel of the new bitmap RGB image in each color plane with pixel values in each color plane which passed the XOR operation. However, the pixels alpha values of the new bitmap image are filled with the pixels alpha values of the bitmap RGB image converted from the acquired image (Original image).

The decryption process of the proposed Android application operates similar to the encryption process. However, the process of the decryption commits the XOR operation before the image pixels scrambling operation and trigger after the user pressed the "Decrypt" button. After either the encryption or the decryption process is completed the application will display the result from the encryption process or the decryption process and prompt for the user to export the result image to the Android device of the user as .png image file.

5.1.4 Results of Encryptions

The proposed Android application in this work capable of encrypting and decrypting the digital image file successfully. Fig. 5.8 shows the result from the encryption process of the proposed Android application which inspected to be the successful encryption. Fig. 9 shows the result from the decryption process with exactly the same password as the password employed in the encryption process which can be inspected that the original image which is encrypted is returned as the result. Fig. 10 shows the result from the decryption process of the proposed Android application with the different password to the password used in the encryption which can

inspected that the result is become more chaotic and possess no evidence of the original image.

The experiment of the encryption strength of the proposed Android application is carried on the password of alphanumeric characters as

Figure 50: The image used in the experiment in this work.

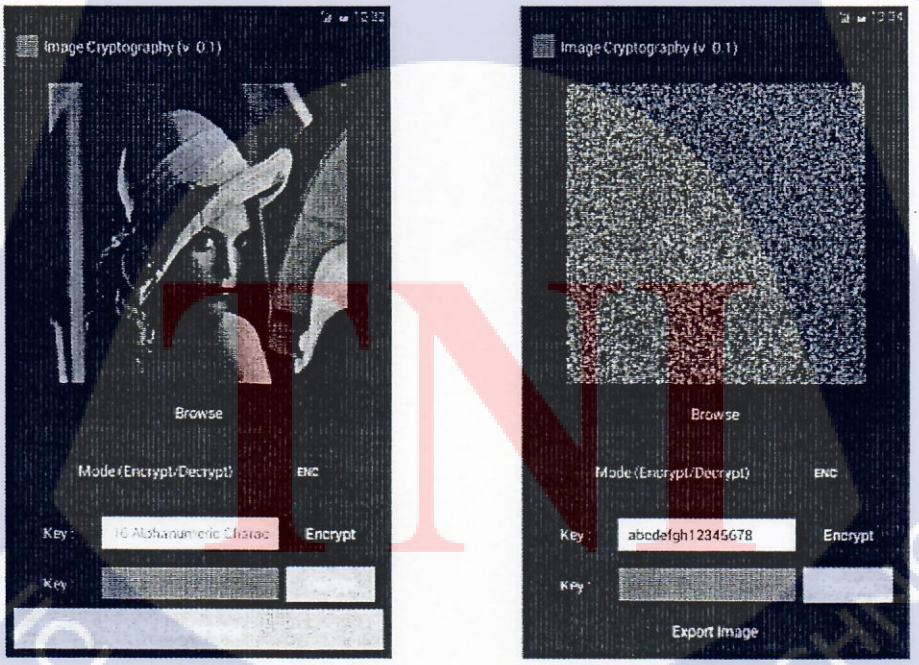

(a) (b)

Figure 51: (a) Before the encryption and (b) after the encryption.

Figure 52: (a) Before the decryption and (b) after the decryption with the same key as the encryption process.

'abcdefgh12345678' for the password in the experiment and the Lena image at the size of 256x256 as displayed in Fig. 5.7 as the image for the experiment and the MATLAB to evaluate the results from the experiment. Fig. 5.8 and 5.9 shows the histogram of the original image and the encrypted image which displays the distribution which is similar to the normal distributed histogram in the histogram of the encrypted image in all color plane; red, green, and blue.

Table 5.3

Comparisons of the Correlation Coefficient of Lena Image at the Size of 256x256

Correlation Coefficient	Value
C_{RR}	0.0069
C_{RG}	-0.0028
C_{RB}	-0.0004
C_{GR}	0.0103
C_{GG}	-0.0027
C_{GB}	-0.0019
C_{BR}	0.0113
C_{BG}	-0.0011
C_{BB}	-0.0032

Table 5.4

the Encryption Time in 256x256 and 512x512 Lena Image between the Absolute Map (1) and the Logistic Map

Chaotic Map	256x256	512x512
Absolute value nonlinearity	6059 ms.	25141 ms.
Logistic	7147 ms.	26773 ms.

Table 5.3 summarizes the correlation coefficients of the encrypted image and for each color planes of the original image compared to the each color plane encrypted image which can be inspected that the correlation coefficients are close to 0 in every pair of the comparison. Table 4 displays the best encryption time which are measured 3 times of the algorithm using (1) and the logistic map which described as

$$x_{(n+1)}=rx_n\,(1-x_n) \qquad (5.10)$$

where r is the control parameter and xn is the condition of the system. The algorithm using (1) can encrypt the image faster than the algorithm using the logistic map. However, the encryption time is longer as the image size increased.

5.1.5 Conclusion

This work has proposed an Android application which is able to encrypt or decrypt the image on an Android device using the chaotic map with absolute value nonlinearity. The application has been tested on an emulator in the ADT plug-in integrated Eclipse IDE. The test results indicate that the application can encrypt and decrypt the test image successfully if the same password is employed in the generation of the initial condition and the control parameter of the chaotic map in the key generation is employed in both encryption and decryption process, and the decryption when the different initial condition of the chaotic map is implemented. In addition, this application also demonstrated that the chaotic maps with absolute value nonlinearity can be implemented in the image cryptography on the Android application development effectively. However, due to some limitations of the Android, the encryption on the images which are larger than 2 million pixels cannot be achieved and also the computation time takes longer as the size of the image increased.

6. CONCLUSIONS

The final report of a research project on "Improvements of Intelligent Electronics System Research Laboratory in the Second Phase" has been presented. The infrastructure and high-technology equipment have been implemented and purchased, including the workbench stations for electronics experiments, high-performance computers, mini-CNC machine, network analyzer, digital multi-meter, and acoustic emission system. Three research themes have been reported, i.e. (i) an intelligent acoustic emission, (ii) intelligent feedback control system, and (iii) intelligent nonlinear dynamic systems for secure communications and data storage. The outputs of research operation are not only publication of research papers but also academic services to industrial sectors.

7. LIST OF PUBLICATIONS

[1] Wimol San-Um and Warakorn Srichavengsup, "*A Robust Hash Function Using Cross-Coupled Chaotic Maps with Absolute-Value Sinusoidal Nonlinearity*", International Journal of Advanced Computer Science and Applications, Vol. 7, No, 1, pp. 602-611, 2016.

[2] Warakorn Srichavengsup and Wimol San-Um, "*Data Encryption Scheme Based on Rules of Cellular Automata and Chaotic Map Function for Information Security*", International Journal of Network Security, Vol. 18, No. 6, pp. 1130-1142, 2016.

[3] Pitchapa Lotrakul, Wimol San-Um and Masaaki Takahashi, "*The Monitoring of Three-Dimensional Printer Filament Feeding Process using an Acoustic Emission Sensor*", EcoDesign 2015 International Symposium, Tokyo, Japan, pp. 624-630, 2-4 December, 2015.

[4] Wimol San-Um, Patinya Ketthong and Jeerana Noymanee, "A Deterministic Node Mobility Model for Mobile Ad Hoc Wireless Network using Signum-Based Discrete-Time Chaotic Map", 2015 International Telecommunication Networks and Applications Conference (ITNAC 2015), Sydney, Australia, pp. 115-120, 18-20 November, 2015.

[5] Sivapong Nilwong and Wimol San-Um, "*An Image Encryption Scheme and Its Android Application using Robust Chaotic Map with Absolute Value Nonlinearity*", The 2nd Management and Innovation Technology International Conference (MITiCON2015), Bangkok, Thailand, pp. 145-149, 16-18 November, 2015.

8. References

[1] K.V. Wong and A. Hemandez, "Review Article: A Review of Additive Manufacturing," ISRN Mechanical Engineering, vol. 2012, Article ID 208760, 10 pages.

[2] F. Sharon, "Additive Manufacturing Technology: Potential Implications for U.S. Manufacturing Competitiveness," Journal of International Commerce and Economics, 2014.

[3] T. Fang, I. Bakhadyrov, M. A. Jafari', and G. Alpan, "On-Line Detection of Defects in Layered Manufacturing," IEEE International Conference on Robotics & Automation Leuven, Belgium, 1998.

[4] H. Rieder, A. Dillhofer, M. Spies, J. Bamberg, and T. Hess, "Online Monitoring of Additive Manufacturing Processes Using Ultrasound," 11th European Conference on Non-Destructive Testing (ECNDT 2014), 2014.

[5] J. Yoon, D. He, and B. V. Hecke, "A PHM Approach to Additive Manufacturing Equipment Health Monitoring, Fault Diagnosis, and Quality Control," Annual Conference of the Prognostics and Health Management Society, 2014.

[6] "Replicator2 Desktop 3D Printer Troubleshooting and Maintenance," MakerBot Industries, Brooklyn, NY.

[7] S. M. A. Al-Obaidi, M. S. Leong, R.I. R. Hamzah, and A. M. Abdelrhman, "A Review of Acoustic Emission Technique for Machinery Condition Monitoring: Defects Detection & Diagnostic," Applied Mechanics and Materials, vol. 229-231, pp. 1476-1480, 2012.

[8] C. K. Tana, P. Irvinga, and D. Mbab, "A comparative experimental study on the diagnostic and prognostic capabilities of acoustics emission, vibration and spectrometric oil analysis for spur gears," Mechanical Systems and Signal Processing, vol. 21, pp. 208–233, 2007.

[9] "LM317 data sheet," STMicroelectronics.

[10] MISTRAS Group, Inc., Phantom power. [Online]. Available: http://www.pacndt.com/index.aspx?go=products&focus=/sensors/phantompower/index.htm

[11] National Physical Laboratory (2012) Guide on Acoustic Emission Sensor Couplants. [Online]. Available:

http://www.npl.co.uk/acoustics/ultrasonics/research/guide-on-acoustic-emission-sensor-couplants

[12] http://www.thingiverse.com/thing:1000086

[13] Krzysztof Jemielniak, "Some aspects of acoustic emission signal pre-processing" Journal of Materials Processing Technology 109 (2001) 242-247

[14] Jiao Yang, Yang Qingxin, Li Guanghai, Zhang Jingyan, "Acoustic emission source identification technique for buried gas pipeline leak" IEEE 2006 1-4244-0342-1/06

[15] M. Noipitak, A. Prateepasen, W. Kaewwaewnoi, "A Relative Calibration Method for Valve Leakage Rate Measurement System" Elsevier Measurement 44 (2011) 211-218

[16] Didem Ozevin, James Harding, "Novel Leak Localization in Pressurized Pipeline Networks using Acoustic Emission and Geometric Connectivity" International Journal of Pressure Vessels and Piping 92 (2012) 63-69

[17] Athanasios Anastasopoulos, Dimitrios Kourousis, Konstantinos Bolas, "Acoustic emission leak detection of liquid filled buried pipeline" Acoustic Emission Group (2009) J. Acoustic Emission, 27

[18] Valeriy N. Ovcharuk, Qin Hongwu, "Hardware-Software Complex for Acoustic Emission Spectral Analyzing" International Siberian Conference on Control and Communications SIBCON (2011), 218-220

[19] A. Prateepasen, W. Kaewwaewnoi, P. Kaewtrakulpong, "Smart Portable Noninvasive Instrument for Detection of Internal Air Leakage of a Valve using Acoustic Emission Signals" Elsevier Measurement 44 (2011) 378-384

[20] N.C. Hii, C.K. Tan, S.J. Wilcox, Z.S. Chong, "An Investigation of the Generation of Acoustic Emission from the Flow of Particulate Solids in Pipelines" Elsevier Powder Technology 243 (2013) 120-129

[21] A. Mostafapour, S. Davoudi, "Analysis of Leakage in High Pressure Pipe using Acoustic Emission Method" Elsevier Applied Acoustics 74 (2013) 335-342

[22] R. Hou, A. Hunt, R.A. Williams, "Acoustic monitoring of pipeline flows: particulate slurries" Elsevier Powder Technology 106 (1999) 30–36

[23] Standard Guide for Detecting the Reproducibility of Acoustic Emission Sensor Response, ASTM Standard No. E976-84.pages/piping-systems.aspx

[24] D. Ozevin and J. Harding, "Novel leak localization in pressurized pipeline networks using acoustic emission and geometric connectivity" International Journal of Pressure Vessels and piping,Vol.92, pp.63-69, 2012.

[25] A. J. Brunner and M. Barbezat, "Acoustic Emission Leak Testing of Pipes for pressurized Gas using Active Fiber Composite Elements as Sensors", Journal of Acoustic Emission, Vol.25, pp. 42- 50, 2007.

[26] Majeed and Murthy, "A model with nonzero rise time for AE signals", Journal of Sadhana, Vol. 25, No.5, pp.465-474, 2001.

[27] P. Davis and J. Brockhurst, "Subsea pipe infrastructure monitoring: A frame work for technology review and selection", International Journal of Ocean Engineering, No. 104, pp. 540-548, 2015.

[28] T. Kaewkongkal and J. Lim, "Statistical estimated parameter for pipeline condition monitoring using acoustic emission", In the proceeding of Instrumentation and Measurement Technology Conference , pp. 1 – 3, 2007.

[29] Ran Wu, Zaiyi Liao and Lian Zhao, WAVELETS APPLICATION ON ACOUSTIC EMISSION SIGNAL DETECTION IN PIPELINE, In the Proceeding of Canadian Conference on Electrical and Computer Engineering, pp. 001211 – 001214, 2008.

[30] L. Sun , Y. C. Li , L. Wang , and J. Wu, "Active Defects Detection and Localization Using Acoustic Emission Method", pp. 5348 – 5351, 2010.

[31] D. Feng, Y. Zheng, T. Nakarada, and Y. Sakurai, "Leakage-Detection System in a Liquid Pipeline", In the proceeding of 8th JFPS International Symposium on Fluid Power, pp.712-717, 2011.

[32] S. L. Ying, L. Y. Bo, S. L. Bo, and L. Ge, "Comparison of Magnetic Flux Leakage (MFL) and Acoustic Emission(AE) Techniques in corrosion Inspection for Pressure Pipelines", In the Proceeding of Chinese Control Conference, pp. 5375 – 5378, 2012.

[33] S. Li, Y. Wen, P. Li, J. Yang, and L. Yang, "Leak Detection and Location for Gas Pipelines Using Acoustic Emission Sensors", In the proceeding of International Ultrasonic Symposium, pp. 957 – 960, 2012.

[34] ASTM E 1316-Standard terminology for nondestructive examinations.

[35] W. Han et al., "Development of a Self-tuning PID Controller based on Neural Network for Nonlinear Systems", Proceedings of the 7th Mediterranean Conference on Control and Automation 1999, pp. 979 – 988

[36] M. Gyun, "Auto-Tuned PID Controller Using a Model Predictive Control Method for the Steam Generator Water Level"., IEEE 2001 pp. 1664 – 1671.

[37] Leila Fallah Araghi et al. "Neural Network Controller Based on PID Controller for Two links- Robotic Manipulator Control", Proceedings of the World Congress on Engineering and Computer Science 2008.

[38] Jin W.M. et al. "application of ANN (artificial-neural-network) in residential thermal control", Eleventh International IBPSA Conference 2009 pp. 64-71

[39] N. Rai and B. Rai, Neural Network based Closed loop Speed Control of DC Motor using Arduino Uno, International Journal of Engineering Trends and Technology 2013, pp. 137 – 140.

[40] Sung-Su Kim and Seul Jung, Hardware Implementation of a Neural Network Controller with an MCU and an FPGA for Nonlinear Systems, International Journal of Control Automation and System 2006, pp. 567 – 574

[41] A. Al-Ghasem and N.Ussaleh, "Air Conditioner Control Using Neural Network and PID Controller", IEEE 2012.

[42] X. Liu, D. zhao and J. Wu, "Frequency-variable air conditioner controller using neural network" , IEEE 2009.

[43] V.Shanmuga Sundaram and T.Jayabarathi, "An artificial neural network approach of load frequency control in a multi area interconnected power system", Elixir Elec. Engg. 38 2011 pp. 4394-4397.

[44] L.iu Luoren, L. Jinling. " Neural Network Modeling of a Tuned PID Controller", Energy Procedia 13 2011 pp. 6988 – 6993.

[45] W. San-Um and S. Nilwong, "The Development of an Android Application for The Chaotic Map with Absolute Value Nonlinearity", MITiCON 2014.

[46] W. San-Um and P. Ketthong, "The Generalization of Mathematically Simple and Robust Chaotic Maps with Absolute Value Nonlinearity", TENCON 2014.

[47] N. K Pareek, V. Patidar, and K. K Sud, "A random bit generator using chaotic maps," International Journal of Network Security, vol. 10, no. 1, pp. 32–38, Jan. 2010.

[48] M. Suneel, "Cryptographic pseudo-random sequences from the chaotic Hénon map," Sādhanā, vol. 34, Part 5, pp. 689–701, Oct. 2009.

[49] L. Gupta, R. Gupta, and M. Sharma, "Low Complexity Efficient Image Encryption Technique Based on Chaotic Map," International Journal of Information & Computation Technology, vol. 4, no. 11, pp. 1029–1034, 2014.

[50] G. A. Sathishkumar, K. B. Bagan, and N. Sriraam, "Image Encryption Based on Diffusion and Multiple Chaotic Maps," International Journal of Network Security & Its Applications (IJNSA), vol. 3, no. 2, pp. 181–193, Mar. 2011.

[51] http://developer.android.com/about/index.html

[52] G. Savithri and K. L. Sudha, "Android Application for Secret Image Transmission and Reception Using Chaotic Steganography," International Journal of Innovative Research in Computer and Communication Engineering., vol. 2, issue 7, pp. 5107-5113, Jul. 2014.

[53] R. Hilborn, "Bifurcation Theory," Chaos and Nonlinear Dynamics: An Introduction for Scientist and Engineers, pp. 106, 2000.

[54] M. Cencini, F. Cecconi, A. Vulpiani, "Characteristic Lyapunov exponents," CHAOS From Simple Models to Complex Systems, pp. 111-126, 2010.

[55] http://developer.android.com/tools/sdk/eclipse-adt.html

[56] http://developer.android.com/tools/devices/emulator.html